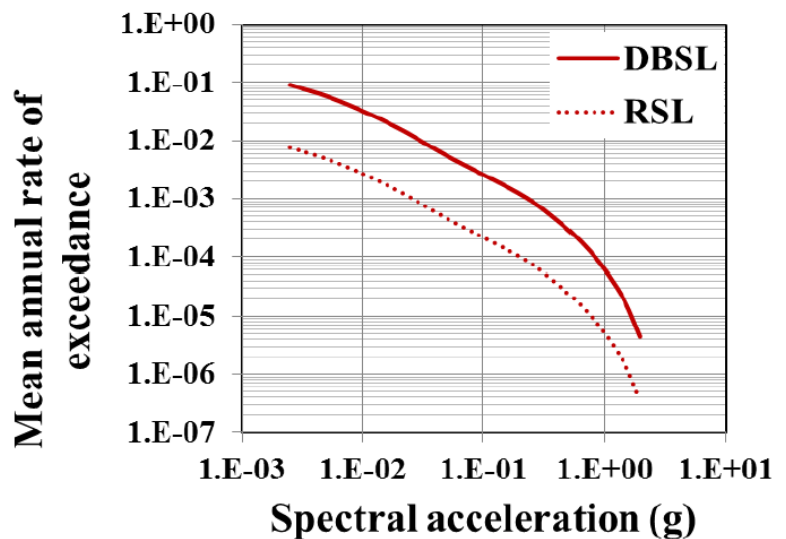# MOUNTAIN-PLAINS CONSORTIUM

MPC 19-383 | C Tucker and L. Ibarra

Seismic Performance of Circular Concrete Filled Steel Tube Columns for Accelerated Bridge Construction

MOUNTAIN-PLAINS
CONSORTIUM REGION 8

Seismic Performance of Circular Concrete Filled Steel Tube Columns for Accelerated Bridge Construction

Catherine Tucker

Luis Ibarra, PhD

Department of Civil & Environmental Engineering
The University of Utah

July 2019

Acknowledgements

Disclaimer

The contents of this report reflect the views of the authors, who are responsible for the facts and the accuracy of the information presented. This document is disseminated under the sponsorship of the Department of Transportation, University Transportation Centers Program, in the interest of information exchange. The U.S. Government assumes no liability for the contents or use thereof.

ABSTRACT

This study evaluates the seismic performance of circular concrete-filled tube (CCFT) columns in accelerated bridge construction (ABC) projects. CCFT components are considered of interest for bridges subjected to seismic forces due to their efficient structural behavior under combined axial and bending loads: lateral stiffness of the steel tube is increased by the concrete, and concrete confinement is provided by the steel tube. This research addresses the ability of CCFT columns to perform adequately under gravitational and seismic loading before the concrete reaches its design strength. A reduced seismic hazard that accounts for this temporal condition is also implemented. Performance evaluation is based on the probability of failure of the CCFT column.

For this research, a Caltrans bridge used in previous Pacific Earthquake Engineering Research Center (PEER) studies is adopted. The performance of a proposed CCFT column was compared to the original circular reinforced concrete (RC) column. Numerical analyses using concentrated plasticity models in OpenSees were used for this evaluation. Experimental data was used to calibrate the deteriorating response of CCFT columns in OpenSees. The analytical model predicts the CCFT column's behavior under monotonic, static cyclic, and dynamic (seismic) loading. Then, the model was adapted to consider the effects of partial concrete compressive strength on the column behavior. The study accounts for temporary conditions, such as concrete compressive strength lower than the design value and reduced seismic loads. Results indicate that CCFT columns with partial design concrete compressive strength can be used for ABC because the relatively low decrease in strength is offset by the reduced seismic loads for this temporal condition.

TABLE OF CONTENTS

LIST OF TABLES

LIST OF FIGURES

LIST OF SYMBOLS

M_c .... maximum moment capacity of system

M_p .... plastic moment of system

M_r .... residual moment (strength) ratio

M_y .... yield moment of system

P .... load applied (can refer to axial or bending load depending upon context)

P_f .... probability of failure

$Pr[\,]$ .... denotes the probability of the event within the brackets

P_y .... axial yielding load, as calculated from AISC (P_n)

PE .... annual hazard curve

P-Δ .... P-Delta (geometric non-linearity effects)

R_n .... nominal bond strength

R_μ .... ductility dependent strength reduction factor

S_a .... spectral acceleration

$S_{a,c}$ .... spectral acceleration at collapse

S_d .... spectral displacement

t .... HSS tube thickness

t_d .... duration of temporary condition

T_1 .... first-mode period of vibration of system

T_n .... natural period of vibration of system

W .... effective seismic weight of system

α_c .... post-capping stiffness ratio / negative tangent stiffness

α_s .... strain hardening ratio

β .... dispersion on collapse capacity due to RTR variability

β_i .... deterioration parameter for excursion

γ .... original deterioration parameter used in Ibarra model, where subscripts s, c, a, k correspond to basic strength, post-capping strength, accelerated stiffness, and unloading stiffness deterioration, respectively

δ_c .... deformation at maximum capacity

δ_{max} .... deformation at maximum capacity

δ_p .... deformation at plastic capacity (associated with monotonic loading)

δ_{pc} .... deformation at post-capping capacity (associated with monotonic loading)

δ_r .... deformation at residual strength capacity

δ_u .... deformation at ultimate capacity

δ_y .... deformation at effective yield capacity

η ....base shear yield strength of the system, F_y, normalized by weight, W

θ ....elastic stability coefficient

θ_p ....plastic rotation capacity

θ_{pc} ....post-capping rotational capacity

θ_{max} ....maximum drift ratio

θ_u ....ultimate rotational capacity

κ ....residual strength ratio

λ ....various: modified deterioration parameter (same subscripts used as for γ), a scale factor used in IDAs, slenderness ratio, mean

λ_{CC}..................mean annual frequency of collapse

λ_{CCFT}...............slenderness ratio of CCFT

λ_{HSS}..................slenderness ratio of HSS

λ_{S_a} ....mean hazard curve

Λ........................deterioration parameter implemented in OpenSees (same subscripts used as for γ)

ξ ....damping ratio of system

σ_{lnS_a} ....standard deviation of the log of the collapse capacity

LIST OF ABBREVIATIONS

AASHTO ....The American Association of State Highway and Transportation Officials

ABC ....Accelerated Bridge Construction

ACI...................The American Concrete Institute

AISC ....The American Institute of Steel Construction

ASCE ....The American Society of Civil Engineers

ASTM ....The American Society for Testing and Materials

Caltrans ....The California Department of Transportation

CCFT ....Circular Concrete Filled (steel) Tube (nomenclature used in this research)

CFST...............Concrete Filled Steel Tube (nomenclature used in other research reviewed herein)

CFT ....Concrete Filled (steel) Tube (can include circular, square or rectangular sections)

DBE ....Design Basis Earthquake

DBSL ....Design Basis Seismic Load

DM ....Damage Measure

DOF ....Degree of Freedom

DOT ....Department of Transportation

EDP ....Engineering Demand Parameter

FC....................Fragility Curve

FEA..................Finite Element Analysis

FEMA ....The Federal Emergency Management Agency

GM ....Ground Motion

HC...................Hazard Curve

HSC..................High Strength Concrete

HSS ....Hollow Structural Section

IDA ....Incremental Dynamic Analysis

IM....................Intensity Measure

LRFD ....Load and Resistance Factor Design

LSD..................Limit States Design

LVDT...............Low Voltage Displacement Transducer

MDOF..............Multiple Degree of Freedom

NPP ....Nuclear Power Plant

PEER................The Pacific Earthquake Engineering Research Center

RC ....Reinforced Concrete

RSL ....Reduced Seismic Load

RTR..................Record to Record (variability)

SCC..................Self Consolidated Concrete

SDOF ....Single Degree of Freedom

SF ....Safety Factor

1. INTRODUCTION

This research evaluates the seismic performance of circular concrete-filled tube (CCFT) columns in accelerated bridge construction (ABC) projects. The objective of ABC is to accelerate the construction schedule. For this reason, current ABC designs usually use precast concrete columns grouted to rebar connections at base and top, if intermediate columns are required. The bridge can be assembled in a few days, but the seismic performance objectives cannot be reached until the columns' top and base connection grout reaches design strength. There are additional issues of concern with the use of precast concrete intermediate columns: the precast connection is difficult to construct because of congestion at the connection splices and potential rebar misalignments. Also, the use of precast columns assumes precast components are readily available, which is not always the case, specifically in emergency bridge construction, one of the primary applications of ABC.

Were CCFT columns to be used instead, the distinct advantage is that connection at the top and bottom of the column is a standard bolted connection — capable of resisting design loads when being bolted, without the need to wait for design strength to be reached. The bolted connection also eliminates the issue of rebar congestion at the connection, faced in the case of the grouted precast column connection, and the materials — steel tubes and concrete — needed to construct CCFT columns are readily available.

The time the CCFT concrete filling takes to cure, and the column's reduced capacity for that duration, poses a primary challenge if CCFT columns are to be considered as a viable alternative for ABC. This study investigates whether a designation of temporary condition can be used to reduce the Design Basis Earthquake (DBE).

A design-basis bridge was selected to evaluate the seismic performance of CCFT columns before the concrete achieved the design compressive strength. It was modeled in OpenSees (McKenna et al., 2000) using a concentrated plasticity model. For validation of the model, experimental data of CCFT columns subjected to static cyclic loading (Marson, 2000) were matched with the analytical model. The model was then used for analysis of the design-basis bridge.

1.1 Background and Motivation

Concrete-filled tubes (CFTs) are steel tubes (e.g., hollow structural sections, HSSs), used as formwork, into which concrete is poured. CFTs have received considerable attention in the engineering community primarily because of their high performance under several failure modes. As compared with unfilled HSSs, CFTs have higher axial capacity, ductility, energy absorption, and fire resistance (Zhao et al., 2010). In addition, CFTs can be constructed using standard structural materials readily available. This makes them ideal to use in remote geographical areas and in cases of emergency construction where other more complex structural assemblies would be either cost or time prohibitive. In addition, the CFT assembly is non-proprietary and is affordable in comparison to assemblies with comparable performance.

The use of CCFT for bridge piers has gained popularity over the past several years. An early comparison between alternatives can be seen in Figure 1.1. The bridge of Figure 1.1c was constructed in Japan in 1982. At that time, concrete filling was used with the objective of increasing the column's strength and expected deflection capacity.

failure of steel bearings

transverse movement of girder

steel beam

inclination

cracks

deformation of cross section

steel column

crack along welded portion

local buckling of stiffened plate

encased concrete against car collision

crack at base

G.L.

cracks of footing concrete

fracture or large deformation of anchor bolts

steel anchor frame

failure or cracks of concrete piles

lateral flow of soil due to liquefaction

(a)

steel beam

hole for casting concrete

encased concrete

composite column

diaphragm with many holes for effective casting of concrete

3000   3000

outer stiffened steel plate

(units : mm)

(b)

23800

3100 500 7800 1000 7800 500 3100

trunk lanes

2000

emergency shoulder

9061

beam member

composite column

11500   11500

(units : mm)

(c)

Figure 1.1 Bridge piers: a) Steel b) CFT c) CCFT (Kitada, 1998)

2

After the Hyogoken-Nanbu earthquake of 1995, CFTs were used in bridge construction because of their ductility. The objective was the fabrication of bridge columns with high ratios of ductile capacity to compressive strength. Using CFTs in bridge construction was an attractive option as an alternative to increasing shear reinforcing in RC columns. (Kitada, 1998)

The current performance objective of highway bridge seismic design is for the superstructure to behave elastically, while the substructure may exhibit inelastic ductile behavior during large seismic events (AASHTO, 2012). With the need for ductile behavior, the use of CCFT for bridge piers is gaining traction.

The list of potential advantages of CCFT for ABC includes: (i) the steel tube provides confinement to the concrete, allowing full composite behavior to develop, which in turn allows greater energy dissipation; (ii) the steel tube acts as formwork for the concrete filling; (iii) the steel tube makes steel reinforcing bars unnecessary; (iv) with the use of weathering steel or proper coatings steel tubes are weather-resistant; (v) the concrete provides continuous buckling resistance for the steel tube, significantly increasing ductility, and thereby the energy dissipation of the column; and (vi) the concrete, through bond with the steel, provides increased capacity through composite action. .

CCFTs are selected for this study because circular cross sectional CFTs are better able to resist multiple cycles of lateral loading, remaining ductile longer than their rectangular counterparts (Kitada, 1991, 1992). Additionally, the circular cross section shape results in superior concrete confinement.

1.2   Statement of Problem

This project addresses the practicality of using concrete-filled steel tubular (CFT) columns for accelerated bridge construction (ABC). Of particular issue with this method is the time it takes for CFT columns to reach design strength relative to the time available before the bridge must be in service. Note that the steel tube alone is strong enough to withstand gravity loads, assuming the concrete only provides lateral support against buckling. The use of a reduced seismic hazard for temporary conditions can be used to shorten the time after which the bridge can be in service.

1.3   Scope and Objectives

This study's scope includes the review of existing literature and research related to CCFT beam-columns, to temporary conditions, and to ABC. Using this background, concentrated plasticity models are created that accurately reflect the behavior results from experimental tests.

The objective of the research is to predict whether CCFT columns can be used in ABC before the concrete reaches the full design strength, without significantly increasing the system's probability of failure. The study generates concentrated plasticity models to reliably predict the nonlinear performance of CCFT components up to the collapse limit state and calibrates for first time the deteriorating nonlinear parameters required for these numerical simulations.

Also, a methodology for determining the probability of failure considering a temporary condition is applied to CCFT columns. Temporary conditions are often used in the nuclear industry, but they are applicable for CCFT columns during the first 28 days because the temporary condition is well-defined and discrete.

1.4   Methodology

This research started with determination of plastic spring parameters for use in a concentrated plasticity analytical model of a CCFT column. They were calibrated by comparison with experimental CCFT hystereses, considering the effects of P-Δ. The proposed CCFT column design was chosen on the basis of its comparable P-M envelope with that of the RC column. Once the CCFT column was designed, and the plastic spring parameters were known, the proposed column was subjected to monotonic, static cyclic, single dynamic loading, and incremental dynamic analyses (IDAs), as a function of concrete age, using a concentrated plasticity model.

The IDAs were performed using 44 far-field ground motions. The failure mode mechanism to be evaluated was the collapse limit state, which can be obtained for the selected CCFT column under dynamic loading for different concrete strengths (3, 7, 14, and 28 days). Fragility curves were developed from the IDAs. A hazard curve is created for Salt Lake City, UT, using a reduced design basis earthquake as a function of the time the concrete core in the CCFT was allowed to cure. Ultimately, the fragility curves and the hazard curve were numerically integrated to obtain the probability of failure for different concrete strength conditions.

2.   LITERATURE REVIEW

This section is divided into i) CFT behavior under seismic loading, ii) CFT concrete strength as a function of time, and iii) temporary conditions.

2.1   Seismic Behavior of Concrete Filled Steel Tube Columns

The concrete core of CFT has two functions: to increase flexural stiffness and ultimate strength, and to prevent local buckling of the steel tube. Whereas a slender HSS is usually limited by buckling failure, the increase in CFT capacity is caused by the added compression strength from the presence of concrete in CFTs, which also provides continuous bracing for the steel tube (Zhao et al., 2010).

Local buckling of a CFT column is significantly reduced from that of an unfilled steel tube column, but it is not eliminated completely. Local buckling mainly depends on the ratio of the outside diameter of the steel tube to its thickness (D/t ratio). Concrete filling increases the buckling threshold as much as 70 percent (Zhao et al., 2010). CCFT columns are selected for this study because they can resist bending forces equally well from any direction due to non-directionality of their circular cross section. CFT columns also have a high strength-to-weight ratio due to confinement of concrete.

2.1.1   Slenderness Ratio

The slenderness ratio for CCFT is defined by AISC (AISC, 2010b) as a function of the type of loading applied and as compared to the same diameter HSS. For the HSS, the slenderness ratio λ_{HSS} is

$$\lambda_{HSS} = \frac{D}{t} \qquad (1)$$

where D is the outer diameter of the steel and t is the thickness of the steel tube.

The CCFT slenderness ratio is defined as

$$\lambda_{CCFT} = C \frac{E_s}{f_y} \qquad (2)$$

where E_s is the modulus of elasticity of the steel

f_y is yielding strength of steel and

C is an empirical coefficient defined by AISC, varying between 0.09 and 0.31 depends on whether axial or bending loading is applied and the CCFT slenderness ratio.

The design equations governing the design of the CCFT are determined depending on how the CCFT slenderness ratio compares to that of the HSS of the equal diameter.

An et al. (2012) investigated the behavior and failure modes resulting from axial compression of slender and thin-walled CCFT columns. They found CCFT columns under axial compression exhibit elastic and elastic-plastic instability failure. They also concluded that the failure mode of slender circular CCFT columns is elastic instability, and concrete strength is less relevant in slender CCFT columns. They confirmed that ultimate strength is determined by the column's flexural rigidity, is inversely related to slenderness ratio, and directly related to steel ratio and concrete strength. Han et al. (2011) also tested

CFT columns under cyclic loading, concluding that column bending and shear capacity are the main failure mechanisms, whereas buckling is usually prevented by the continuous lateral support of the concrete.

2.1.2   Concrete Confinement

The axial and flexural strength of a CFT column is greater than that of either an equivalent concrete column or of an unfilled steel tube column, due to concrete's tendency to have a higher Poisson ratio than steel at high loads (Ranzi et al., 2013). That is, the steel tube confines the concrete and prevents transverse expansion of the concrete. As the stresses in the column increase, the concrete transverse expansion amount increases, and the confinement effect provided by the steel is magnified. This confinement then serves to equivalently increase the axial strength of CFT columns, particularly for shorter columns.

Knowles and Park (1969) investigated the effect of slenderness ratio on axial strength of CFT columns and found that slenderness ratio plays a role in concrete confinement. They concluded for a slenderness ratio of less than 35, concrete confinement is ensured.

2.1.3   Composite Action

Composite action allows CFT columns to resist buckling, have good ductility, and high axial resistance. Composite action relies on bond behavior at the steel-concrete interface, which according to AISC (2010b), can be estimated as:

$$R_n = 0.25\pi D^2 C_{in} F_{in} \qquad (\,3\,)$$

Where:

R_n is nominal bond strength, in kips

D is the outside diameter of the HSS, in in.

C_{in} = 2 if the filled composite member extends to one side of the point of force transfer, or 4 if the filled composite member extends on both sides of the point of force transfer

F_{in} is nomimal bond stress = 0.06 ksi

and for LRFD, φ = 0.45

This formula incorporates the two types of bond transfer: circumferential, $0.25\pi D$, and longitudinal, DC_{in}. The bond stress value is a lower bound adopted from experimental data. However, some experimental tests have shown that the entire circumference can contribute to circumferential bond (Zhang et al., 2012).

Zhang et al. proposed new formulas, based on finding a correlation between bond behavior and the cross-sectional dimensions of the CFT, and extant experimental data from push-out, push-off, and connection tests. They posited that transfer length, dictating longitudinal bond behavior, varies according to material and geometric properties, and can increase axial load capacity. The transfer length used in design calculations must address two limit states: slip along the entire length of the column and local slip near the point of load application.

Experimental results show that in the case of a column with at least two girders framing into opposite sides, bond stresses are developed around the entire perimeter (Zhang et al., 2012). They also found that it is justified to use the entire circumference as the bond length for corner columns, because they are exposed to higher bending moments that increase concrete confinement and, therefore, bond strength. The following design equations were then proposed:

$$R_n = \pi D L_{bond} F_{in} \qquad (4)$$

$$L_{bond} = C_{in} D \qquad (5)$$

$$F_{in} = 30.7 \left(\frac{t}{D^2}\right) \leq 0.2 \qquad (6)$$

Where the variables remain the same as in Equation (3), but:

L_{bond} is length of the bond region, and

t is the design wall thickness of the steel section, in in.

The LRFD resistance factor, φ, was calculated as 0.55, but it was recommended to continue using 0.45.

Composite action between the steel tube and concrete is affected by concrete curing — concrete shrinkage that may delaminate the surface of the concrete from the tubular member. For this research, bond associated with composite action is assumed to be 100 percent, regardless of concrete curing time, but the effects of concrete curing on bonding, and by association on composite action, is an area of future research.

2.2 Time-dependent Behavior of Concrete

Understanding the concrete strength gain of CFT columns as a function of concrete age and the associated bonding behavior is critical to determining when a bridge can be placed safely in service. Unfortunately, most available studies are not focused on the short time during which concrete strength gain is attained, but longer term measurements.

Because concrete is pumped into the steel tubes, its exposure to air is minimal, affecting its ability to dry as part of the curing process. This sealed condition may affect creep and shrinkage processes. Using creep coefficients ranging from 50–60 percent of the typically recommended values conservatively predicts experimental findings (Ranzi et al., 2013). For this research, creep is not of central concern as creep is a long-term process and is not expected to affect column behavior during the first 28 days.

For typical concrete mixes, drying shrinkage is significantly different for CCFT from typical concrete exposed to air, while autogenously shrinkage is not affected by the lack of exposure to air. Experiments were conducted on CCFT specimens allowed to cure long-term, unloaded. The amount of shrinkage measured was small, and some studies have suggested shrinkage may be neglected for CCFT (Ranzi et al., 2013).

Creep and shrinkage result in stress redistribution at the interface between the steel tube and the concrete filling. Usually perfect bond/composite behavior is assumed between the steel and concrete. Then full shear interaction theory can be applied in analysis of the column, showing good agreement with experimental results of long-term measurements. The effect of creep on ultimate axial strength of CCFT

is not clear. Some researchers found that creep reduces the carrying capacity for up to 20 percent, whereas others found that creep has no effect (Ranzi et al., 2013).

The effect of concrete confinement in CCFT is increased further by the low level of shrinkage exhibited by CCFT. However, experimental findings may over predict confinement because the loading is commonly applied to the concrete, not the steel or the entire composite section (Ranzi et al., 2013).

2.3   Temporary Conditions

Temporary conditions will be investigated for use in the period of time before the concrete has achieved full design strength. In the case of ABC projects, reducing curing time through use of concrete accelerating admixtures could be disadvantageous.

One of the most common accelerating admixtures used is calcium chloride ($CaCl_2$). In addition to accelerating strength gain, it increases drying shrinkage and steel corrosion (Kosmatka and Panarese, 2002), both which pose problems for CCFT. Drying shrinkage reduces bond strength and composite action, and therefore, ductile behavior. Due to concrete in CCFT being encapsulated from air, drying shrinkage will not be as significant as in other types of construction, but no studies have been done to quantify the effects of drying shrinkage. Steel corrosion can also affect the external tube surface, and more critically, the interior of the tube, where it can be potentially undetected. The alternative to accelerating strength gain is to address the performance of CFT columns under gravitational and seismic loading before conventional concrete reaches its design strength and consider the seismic hazard risk reduction due to this temporary condition.

Cornell and Bandyopadhyay (1996) evaluated several scenarios in which nuclear facilities might have reduced seismic design loads. Methods for determining reduced seismic loads fall into categories of intermittent load combinations, probability of failure argument, and the risk averaging argument.

Temporary conditions are currently used in nuclear facilities, but there is ambiguity about what constitutes a temporary condition (Hill, 2004). By contrast, temporary conditions for CFT in ABC are well-defined, having an upper limit for the temporary condition designation: after the concrete reaches its design strength, the temporary condition is discarded. Temporary conditions can be considered by applying a reduced seismic load (RSL) during the duration of the temporary condition.

Reduced hazard levels for temporary conditions have been investigated for several loading conditions. Boggs and Peterka (1992) created a model to represent the probability of a wind speed resulting in structural failure of a temporary structure. They derived a correlation between the design recurrence interval of a permanent structure and that of a temporary one. The correlation was derived by first evaluating the failure probability of permanent structures due to high wind speed. The probability of failure was defined in terms of the probability of a wind speed exceeding that wind speed whose magnitude resulted in structural failure.

To obtain adequate safety for temporary conditions, Boggs and Peterka (1992) indicated that either the safety factor, SF, must be increased, or the mean recurrence interval of the design wind speed for temporary structures must be increased. The study mentions that the methodology presented is imprecise and not a good predictor of recurrence interval for increasingly short periods of less than a year. This issue is relevant for CCFT in ABC, in which temporary conditions would be of significantly shorter duration than a year.

In response to the paper by Boggs and Peterka, Hill (2004) questioned the logic and safety of allowing reductions in design load due to conditions that are evaluated as temporary, but may be permanent loading conditions. Hill acquiesced there are legitimate temporary conditions that can benefit from design load reductions during the duration of the temporary condition. This is the case in CCFT construction, which has a defined upper limit for the temporary condition designation. After the concrete reaches the design strength, the temporary condition is discarded. In the situation of civil bridge construction, the design strength should be assumed, in the most general case, to take 28 days to reach. In the case of ABC projects, when accelerated construction is the primary desired objective, the 28 days become a significantly long period of time.

Amin et al. (Amin and Jacques, 1994, Olson et al., 1994) evaluated seismic loading for temporary conditions in nuclear power plants. They used annual seismic hazard curves to determine acceleration levels corresponding to temporary loads in which the corresponding acceleration is dependent on the duration of the temporary loading. They reduced the mean annual hazard curve at the site to account for a temporary condition. In this approach, the probability of exceedance in the hazard curve is reduced by a linear proportion based on the temporary condition duration.

Starting with seismic acceleration at the site having a probability distribution function of:

$$F_A(a) = \Pr[A \leq a] \qquad (7)$$

where

A is the random site peak horizontal acceleration

a is the specific value of an acceleration

$F_A(a)$ is the probability distribution function

and Pr[ ] denotes the probability of the event within the brackets – in this case the probability that any particular event a will exceed the peak value A.

Amin et al. then concluded that:

$$PE(t_d, a) = t_d PE(1, a) \qquad (8)$$

where

PE is the annual hazard curve

t_d is the duration of the temporary condition

As is indicated, t_d is multiplied by the annual hazard curve, resulting in a new scaled annual hazard curve.

Amin et al. (1999) also proposed a methodology of applying reduced seismic loads (RSLs) for evaluation of temporary conditions using design basis-allowable loads in nuclear power plants. The design basis seismic event recurrence interval for a temporary condition is specified, through use of a reduced seismic load, such that the probability of failure is the same as in traditional design of permanent structures. This

method posits that design basis earthquakes (DBE) may be considered to be assumed reduced for the period of the temporary condition.

The nature of the temporary condition must be investigated to obtain magnitude of the seismic level needed. The key is how well-defined the time period is for the designation of temporary condition. In this research, the temporary condition vanished when concrete reached the design strength. In nuclear applications, however, temporary conditions may regularly occur through maintenance of the plant.
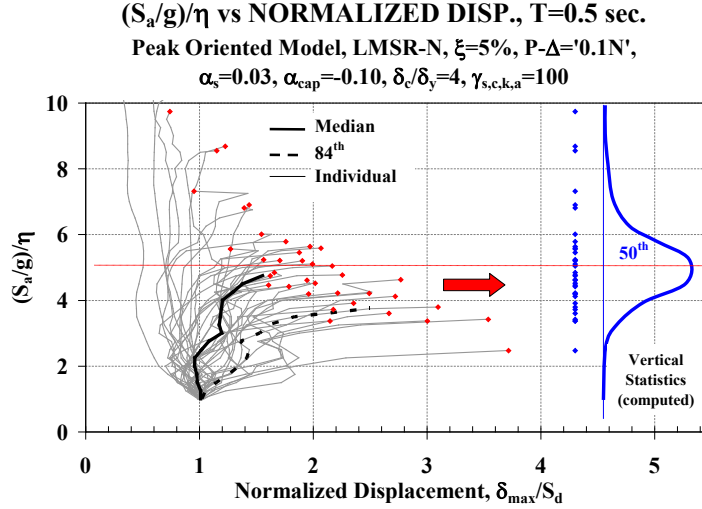
2.4   Collapse Capacity

For this research, the main CCFT column limit state was collapse. Global collapse under seismic excitations refers to the inability of a structural system to support gravity loads in the presence of lateral forces. In recent years, deterioration models and experiments were used to evaluate structural collapse (Ibarra and Krawinkler, 2005, Lignos and Krawinkler, 2012, Villaverde, 2007) and considered record-to-record (RTR) variability as the only source of uncertainty affecting variance of the structural response.

A limited number of studies have evaluated the effect of uncertainty in modeling parameters on collapse capacity for single degree of freedom (SDOF) systems (Ibarra and Krawinkler, 2005, Liel et al., 2009). The level of uncertainty of modeling parameters can be large because of their intrinsic aleatory variability and especially the inability to accurately evaluate them (i.e., epistemic uncertainty).

For modeling collapse capacity of CCFT, evaluation should be based on structural analyses that incorporate deterioration characteristics of structural components subjected to cyclic loading and the inclusion of geometric nonlinearities (P-Δ effects). For SDOF systems, P-Δ effects are usually included by rotating the backbone curve based on a parameter known as the elastic stability coefficient, θ (Adam et al., 2004, Bernal, 1987, Jennings and Husid, 1968, MacRae, 1994, Sun et al., 1973, Vian and Bruneau, 2001).

The development of hysteretic models that include strength and stiffness deterioration (Ibarra et al., 2005, Sivaselvan and Reinhorn, 2000, Song and Pincheira, 2000) improved the assessment of collapse capacity. Collapse of SDOF systems is assumed to occur when the loading path is on the backbone curve and the restoring force approaches zero. Thus, collapse requires the presence of a backbone curve branch with negative slope, a condition caused by P-Δ effects and/or a negative tangent stiffness branch of the hysteresis model. Collapse capacity can be expressed in terms of a relative intensity $(S_a/g)/\eta$, where S_a is the 5 percent damped spectral acceleration at the elastic period of the SDOF system (without P-Δ effects), and $\eta = F_y/W$ is the base shear yield strength of the system, F_y, normalized by weight, W. In this study, however, the structural system is defined, and the intensity measure (IM) is the spectral acceleration at the first period of the system, $S_a(T_1)/g$. IM is a ground motion parameter that can be monotonically scaled by a non-negative scalar (Vamvatsikos and Cornell, 2002).

Nonlinear time history analyses are conducted for increasing $S_a(T_1)/g$ values until the system response becomes unstable. This approach is named Incremental Dynamic Analysis (IDA) (Vamvatsikos and Cornell, 2002). Using IDAs, collapse can be visualized by plotting the intensity measure against an engineering demand parameter (EDP) of interest. For instance, Figure 2.1 presents individual and statistical relative intensity – normalized displacement curves, $(S_a/g)/\eta$ vs δ_{max}/S_d. The deterioration characteristics of the system cause individual curves to eventually approach a zero slope as $(S_a/g)/\eta$ increases. The last point of each individual curve represents the system "collapse capacity", $(S_{a,c}/g)/\eta$. The U.S. Federal Emergency Management Agency (FEMA) adopted IDA as the method of choice for determining collapse capacity (ATC, 2000a, b).

(S$_a$/g)/η vs NORMALIZED DISP., T=0.5 sec.
Peak Oriented Model, LMSR-N, ξ=5%, P-Δ='0.1N',
α$_s$=0.03, α$_{cap}$=-0.10, δ$_c$/δ$_y$=4, γ$_{s,c,k,a}$=100

Figure 2.2 (S$_a$/g)/η – EDP Curves for Baseline SDOF Systems (Ibarra and Krawinkler, 2005)

2.4.1 Scaling of the Ground Motion Records

The most common IM is five percent damped spectral acceleration at the structure's fundamental period of vibration, $S_a(T_1)/g$. To account for RTR variability, the 44 ground motion (GM) records from FEMA P695 (ATC, 2009) were used in this study. Because the IM is $S_a(T_1)/g$, the records were scaled at the S_a/g of the first period of the system:

$$\frac{S_a/g}{F_y/W} = 1 \qquad\qquad (9)$$

where

S_a is $S_a(T_1, 5\%)$

g is standard gravity

F_y is the yielding strength of system, and

W is the effective seismic weight of the system.

2.4.2 Hysteretic Models

The CCFT columns of this study had to be represented with hysteretic models that account for strength and stiffness deterioration. Sivaselvan and Reinhorn (2000) developed a smooth hysteretic model, which allows for deterioration in strength and stiffness and provides for pinching behavior, but it does not include a negative backbone tangent stiffness. Song and Pincheira (2000) proposed a model based on energy dissipated. This model represents cyclic strength and stiffness deterioration and its back bone curve has a post-capping negative tangent stiffness and a residual strength branch. However, the backbone curve cannot account for strength deterioration prior to reaching peak strength. This study uses the hysteretic models developed by Ibarra et al. (2005), which include four deterioration modes: basic strength, post-capping strength, unloading stiffness, and accelerated reloading stiffness deterioration. Ibarra et al. (2005) developed bilinear, peak-oriented, and pinching models, but only peak-oriented models were used in this study.

2.4.2.1 Backbone Curve Model

The backbone curve, shown in Figures 2.3 and 2.4, defines deformation response for a loading protocol, which increases monotonically until collapse. If there is no deterioration, it consists of an elastic stiffness K_e, a yield strength F_y, and a strain hardening stiffness K_s. If deterioration is considered, the curve continues along the slope of K_s until reaching the strength at which the strain hardening interval is capped at a maximum strength F_c. The negative tangent stiffness $K_c = \alpha_c K_e$ (also called post-capping stiffness) continues until the residual strength, F_r, is reached - if one is specified. The displacement associated with the peak strength is normalized as δ_c/δ_y, and may be viewed as a monotonic "ductility capacity."
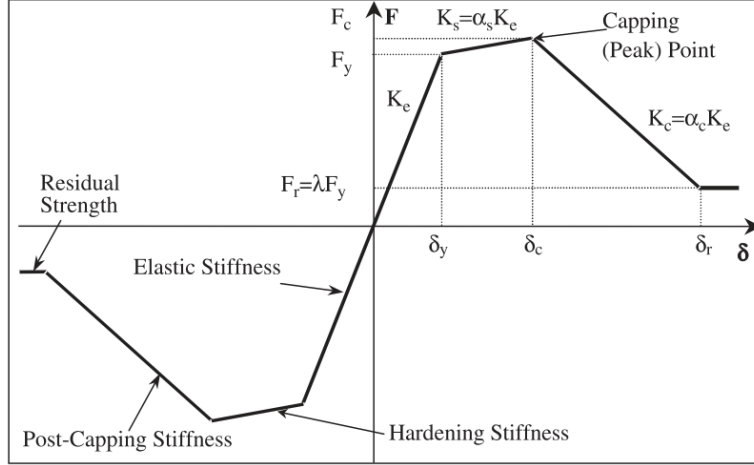
Figure 2.3 Backbone Curve for Hysteretic Models (Ibarra et al., 2005)
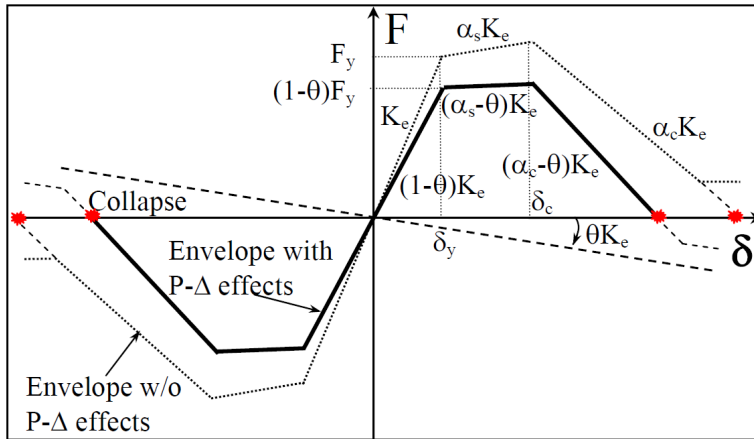
Figure 2.4 Backbone Curves for Hysteretic Models with and without P-Δ (Ibarra and Krawinkler, 2005)

The effect of P-Δ is to rotate the backbone curve in accordance with the elastic stability coefficient, θ. Figure 2.3 illustrates the backbone curve of this model with and without the effect of P-Δ.

$$\theta = \frac{W\delta_y}{F_y h} \qquad (\,10\,)$$

where W is the seismic weight of the system, and h is the height of the system.

2.4.2.2 Peak-Oriented Hysteretic Deterioration Model

The peak-oriented model used in this study to represent nonlinear CFT behavior (Ibarra et al., 2005) has the same rules of the peak-oriented model proposed by Clough and Johnston (1966). The deterioration of reloading stiffness for a peak-oriented model occurs once the horizontal axis is reached (points 3 and 7 in Figure 2.4), and the reloading path targets the previous maximum displacement. The model proposed by Ibarra et al. (2005) can also account for residual strength.
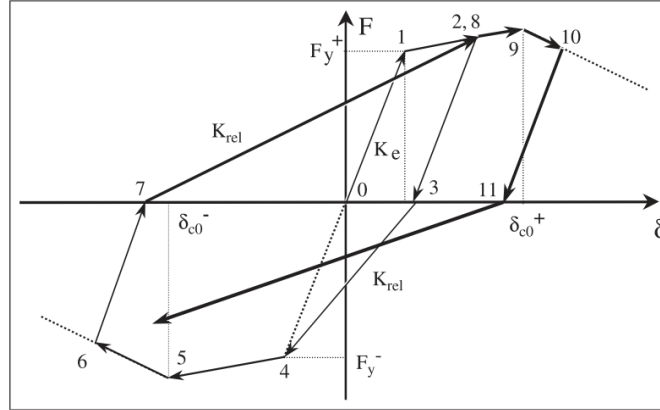
Figure 2.5 Peak-oriented Hysteretic Model (Ibarra et al., 2005)

The hysteretic model includes four modes of cyclic deterioration based on energy dissipation. As observed in Figures 2.5 and 2.6, basic strength and post-capping strength deterioration effects translate the strain hardening and post-capping branch toward the origin, unloading stiffness deterioration decreases the unloading stiffness, and reloading (accelerated) stiffness deterioration increases the target maximum displacement.
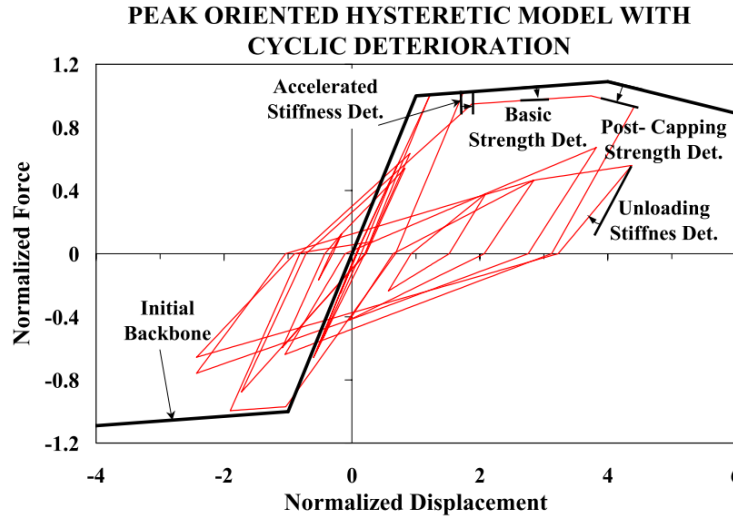
Figure 2.6 Cyclic Deterioration in a Peak-oriented Model (Ibarra and Krawinkler, 2005)
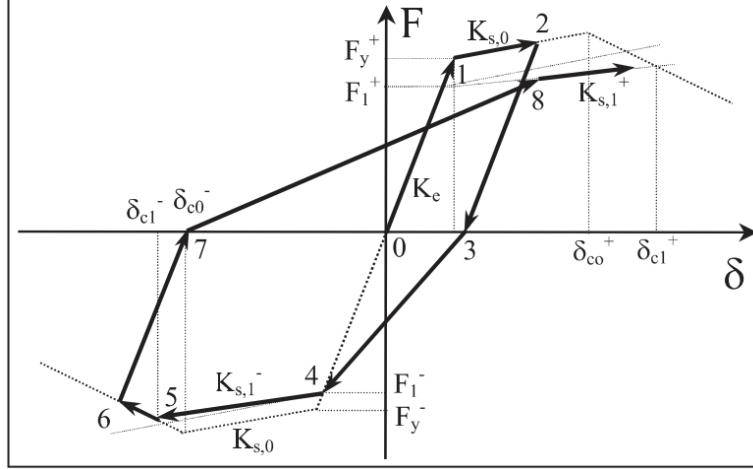
Figure 2.7 Basic Strength Deterioration for Peak-oriented Hysteretic Model (Ibarra et al., 2005)

As is illustrated in Figure 2.6, strength deterioration occurs between points 3 and 4 as a function of the basic strength deterioration rule, which affects a system prior to it reaching its capping stiffness.

The amount of deterioration depends on the parameter β_i, which may be different for each cyclic deterioration mode. For instance, the unloading stiffness in the ith excursion ($K_{u,i}$) is deteriorated as:

$$K_{u,i} = (1 - \beta_{k,i})K_{u,i-1} \qquad (11)$$

where $\beta_{k,i}$, is the deterioration parameter for unloading stiffness in the ith excursion. In its general form, β_i is expressed as:

$$\beta_i = \left(\frac{E_i}{E_t - \sum_{j=1}^{i} E_j}\right)^c \qquad (12)$$

where E_i is hysteretic energy dissipated in excursion i, $\sum E_j$ is hysteretic energy dissipated in previous positive and negative excursions,

$$E_t = \gamma F_y \delta_y \qquad (13)$$

is the reference hysteretic energy dissipation capacity of component in the original Ibarra-Krawinkler model (Ibarra et al., 2005),

The parameter γ for each deterioration mode is calibrated from experimental results. Reasonable results can be obtained if all cyclic deterioration modes are represented by a single parameter $\gamma_{s,c,a,k}$, where the subscripts s, c, a, k correspond to basic strength, post-capping strength, accelerated stiffness, and unloading stiffness deterioration, respectively.

The parameter c was 1 for this study, implying a constant rate of deterioration. The yield deformation was $\delta_y = F_y/K_e$, δ_c, and is cap deformation (deformation associated with F_c for monotonic loading, used in the Ibarra-Krawinkler model), and δ_p is plastic deformation capacity (used in the Lignos-Krawinkler model, discussed below).

2.4.2.3 Modified Hysteretic Model

A modified version of the deteriorating hysteretic model (Lignos and Krawinkler, 2012) developed by Ibarra et al. (2005) was implemented in OpenSees (McKenna et al., 2000) to account for nonlinear rotational behavior (referred to in this paper as Lignos-Krawinkler model). Where equation (13) was used for the Ibarra et al. model,

$$E_t = \lambda F_y \delta_p = \Lambda F_y \quad (14)$$

is the reference hysteretic energy dissipation capacity of component in the Lignos-Krawinkler model (Lignos and Krawinkler, 2012). The central difference is in the parameters λ or Λ used instead of γ, to account for the underlying difference between δ_p and δ_y where $\delta_p = \delta_c - \delta_y$ as illustrated in Figures 2.7 and 2.8. As in the Ibarra et al. model — where the parameter γ is assigned subscripts to represent types of strength deterioration — for the OpenSees model used in this research, the parameters representative of the respective strength deterioration types are:

Λ_s, basic strength deterioration

Λ_c, post capping strength deterioration

Λ_a, accelerated strength deterioration

Λ_k, unloading strength deterioration

This modified peak-oriented hysteretic model (Figure 2.7) was used to model the equivalent stiffness as a spring in the concentrated plasticity model within OpenSees.
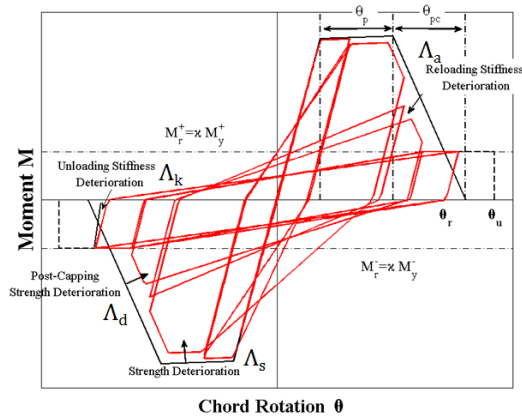
Figure 2.8 Parameters for Peak-oriented Hysteretic Lignos-KrawinklerModel after (Lignos, 2012)
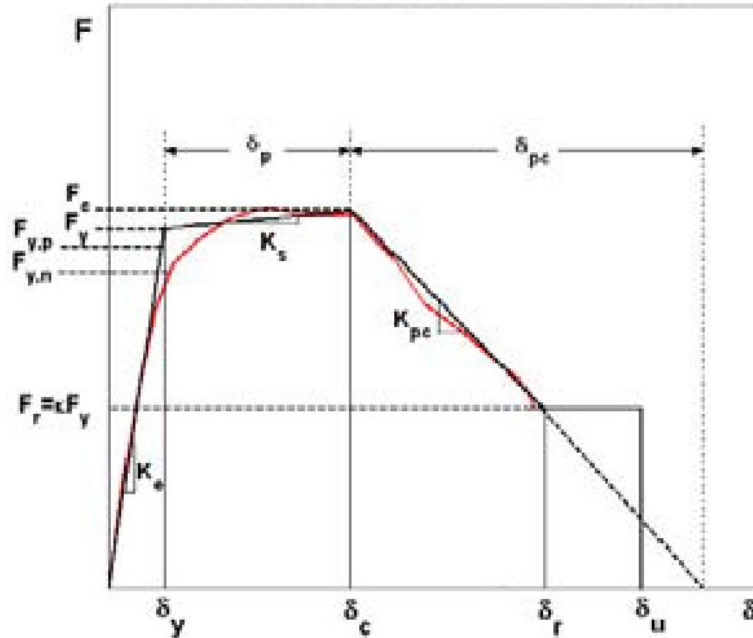
δ_c = cap deformation (deformation associated with F_c for monotonic loading)
F_y = effective yield strength, incorporating "average" strain hardening
δ_y = effective yield deformation (= F_y/K_e)
K_e = effective elastic stiffness
F_r = residual strength capacity
δ_r = deformation at residual strength
δ_u = ultimate deformation capacity
δ_p = plastic deformation capacity associated with monotonic loading
δ_{pc} = post-capping deformation capacity associated with monotonic loading

F_c/F_y = post-yield strength ratio
F_{yp} = predicted effective yield strength (predicted from measured material properties)
F_{yn} = nominal effective yield strength (predicted from nominal material properties)

κ = residual strength ratio = F_r/F_y

Strain hardening ratio $\alpha_s = K_s/K_e = [(F_c/F_y)/\delta_p]/K_e$
Post-capping stiffness ratio $\alpha_c = K_{pc}/K_e = (F_c/\delta_{pc})/K_e$
F_c = strength cap (maximum strength, incorporating "average" strain hardening)

Figure 2.9 Parameters for Backbone Curve for Lignos-Krawinkler Model (Lignos and Krawinkler, 2012)

16

2.4.2.4 Cyclic Deterioration Parameter Values

Ibarra et al. and Lignos and Krawinkler matched their cyclic deterioration parameters to experimental data to determine the reasonable range of numerical values for cyclic deterioration parameters (Ibarra and Krawinkler, 2005, Lignos and Krawinkler, 2012).

For the Ibarra et al. model,

a) no cyclic deterioration: $\gamma_{s,c,a,k} = \infty$

b) slow cyclic deterioration: $\gamma_{s,c,a} = 100$ and $\gamma_k = 200$

c) medium cyclic deterioration: $\gamma_{s,c,a} = 50$ and $\gamma_k = 100$

d) rapid cyclic deterioration: $\gamma_{s,c,a} = 25$ and $\gamma_k = 50$

Steel can be modeled with $\gamma_{s,c,a,k} \cong 130$ and RC modeled with $\gamma_{s,c,a,k} \cong 50$.

Lignos proposed equations from results of a parameter study to determine ranges of numerical values. His study looked at a great number of samples, and based on these results, for HSS one can assume $\Lambda_{s,c,a,k}$ values around 0.3 correspond to rapid deterioration and around 2.8 correspond to slow deterioration. Likewise, for W sections, values around 0.8 correspond to rapid deterioration and around 3 correspond to slow deterioration. For RC, values around 0.5 correspond to rapid deterioration and around 3 correspond to slow deterioration (Lignos and Krawinkler, 2011, 2012).

3. ANALYSIS OF EXPERIMENTAL CIRCULAR CONCRETE-FILLED STEEL TUBE COLUMNS

Extensive experimental databases exist for CCFT. However, cyclic loading experimental data of normal strength CCFT of appropriate dimensions and boundary conditions for highway bridges are scarce.

Among the most recent well-compiled experimental databases for CCFT are those from Goode (2013) and Leon et al. (2011). However, the available database is quite limited for a specimen possessing bridge column characteristics, such as normal strength circular steel tube, normal strength concrete filling, relatively large D/t ratio, fixed base condition, and constant axial load of appropriate P/P_y value. The experimental data with the specimens most closely applicable to the determination of highway bridge parameters included the three experiments described below.

Boyd et al. (1995) performed static cyclic tests on five CCFT with constant axial load. The columns had a diameter of 203.2 mm and relatively large D/t ratios of either 106 or 73. Researchers concluded that the steel tube thickness and addition of steel studs increased energy dissipation. The steel studs reduced deterioration at large deformations. However, these specimens included HSC that resulted in less ductility, greater degradation, and less energy dissipation than normal strength concrete.

Elremaily and Azizinamini (2002) performed tests closely related to current research in terms of D/t ratios and loading protocol, but with the parameters they wanted to consider (high strength concrete, and various P/P_y ratios), only one of their specimens could have been used in this study.

Tests from Marson and Bruneau (2004) were selected for this research because they include the main characteristics of CCFT bridge columns. Marson and Bruneau (2004) tested four columns (CFST64, CFST51, CFST34, and CFST42) under static cyclic loading protocols. These specimens have characteristics expected in highway bridges, such as relatively large D/t ratios, fixed base condition, normal strength concrete, and constant axial load of appropriate P/P_y values. They performed inelastic static cyclic tests until rupture of the steel tube, all which reached 7 percent drift prior to rupture.

They determined specimen sizes after compiling parameters from more than 1,200 highway bridges. Digits at the end of CFST64, CFST51, CFST34, and CFST42 refer to the nominal D/t, which differs from the measured D/t. Slenderness ratios of less than 35 were selected based on the research of Knowles and Park (1969), and P/P_y ratios were also based on the bridge database. The cyclic loading protocol is shown in Figure 3.1.
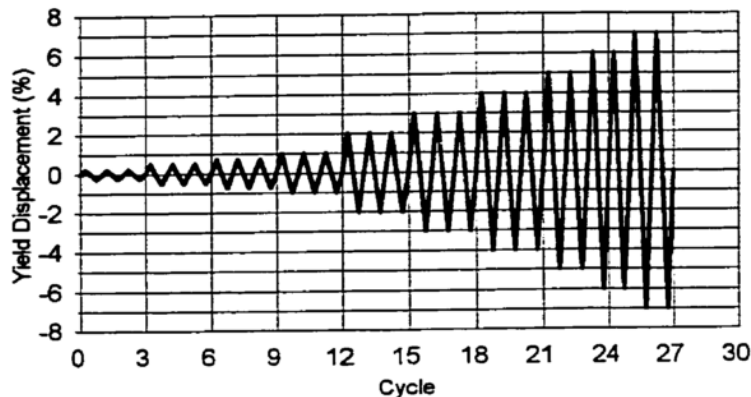
Figure 3.10 Static Cyclic Loading Protocol for Marson and Bruneau Tests (Marson, 2000)

The tested specimens showed local buckling at about $2.0 - 3.0\delta_y$, which coincided with the highest applied lateral force. Hysteretic pinching behavior was observed in CFST64; its larger D/t ratio is indicative of a larger contribution to behavior from concrete, which is best represented as between a peak-oriented and pinching hysteretic model. Tests were stopped at a cycle of $7.0\delta_y$, where necking of steel-tube and significant concrete cracking was observed (Marson and Bruneau, 2004).

The columns were opened after the testing. The concrete in the columns' base was pulverized but was intact at the upper face of the foundation. Researchers indicated that concrete directly below and above the buckled area remained intact, which shows that concentrated plasticity models should provide a reasonable numerical approximation. Hysteretic degradation parameters have been derived for steel and RC components, but the parameterization did not exist for CCFT columns. The degradation parameters were determined by curve-fitting the OpenSees analytical concentrated plasticity model with the Marson Bruneau experimental data. A data summary of these experimental columns is shown in Table 1 (see Appendix A for the rest of the data). Note that Table 3.1 also presents the proposed CCFT column data based on the column design described in the next section.

**Table 3.1** Summary of Proposed CCFT and Marson Bruneau Experimental Data

Column Properties	Proposed CCFT	CFST64	CFST51	CFST34	CFST42
ratio of tube diameter to thickness D/t	64.0	73.9	58.9	43.2	42.8
Outside tube diameter, D (in)	39.0	16.0	12.8	12.8	16.0
Column height, h (in)	264	86.6	86.6	86.6	86.6
f'_c (ksi)	5.2	5.4	5.1	5.9	5.1
F_y (ksi)	50.0	64.1	58.0	60.2	73.2
EI_{eff} (AASHTO) (k-in^2)	5.75E+08	1.50E+07	6.90E+06	8.55E+06	2.11E+07
Reduction of EI_{eff} used for model	none	80%	80%	80%	80%
A_s/A_c	6.6%	5.6%	7.2%	9.9%	10.0%
P/P_y	0.19	0.14	0.34	0.30	0.18
M_y (empirical) (k-ft)	6039	450	271	332	722
M_c (M_c/M_y=1.3) (k-ft)	7851	585	353	431	939
θ, Stability coeff. ($P\Delta/Vh$)	0.072	0.047	0.163	0.150	0.061

4. DESIGN OF A CIRCULAR CONCRETE FILLED STEEL TUBE COLUMN

A Caltrans bridge was selected for this research from a set of benchmark bridges used in PEER studies. The original circular RC columns were replaced by CCFT columns with similar interaction diagrams. Numerical analyses using concentrated plasticity models were used for this evaluation. These analyses were verified through modeling of published experimental data.

4.1 Design Basis Bridge

In 2004, PEER funded a study of seismic performance of highway bridges in California (Ketchum et al., 2004). The researchers selected bridge types to represent the most common highway bridge types employed by Caltrans. For this research, bridge type 1A of this study was adopted (Figure 4.1). The bridge consists of five straight spans with lengths of 120, 150, 150, 150, and 120 ft. The deck consists of post-tensioned cast-in-situ 39 ft. wide, 6 ft. deep concrete box girders to allow two 12 ft. lanes for traffic, a 4 ft. left shoulder, an 8 ft. right shoulder, and traffic barriers at the perimeter. The single column piers are 4 ft. diameter RC columns 22 ft. tall. Data for the design-basis bridge RC column is shown in Table 4.1. A buckling analysis for the proposed CCFT according to AISC (2010a, b) and AASHTO (2012) specifications and a buckling analysis of the RC column according to ACI (2008) specifications is presented in Appendix B.

(a)

(b)   (c)
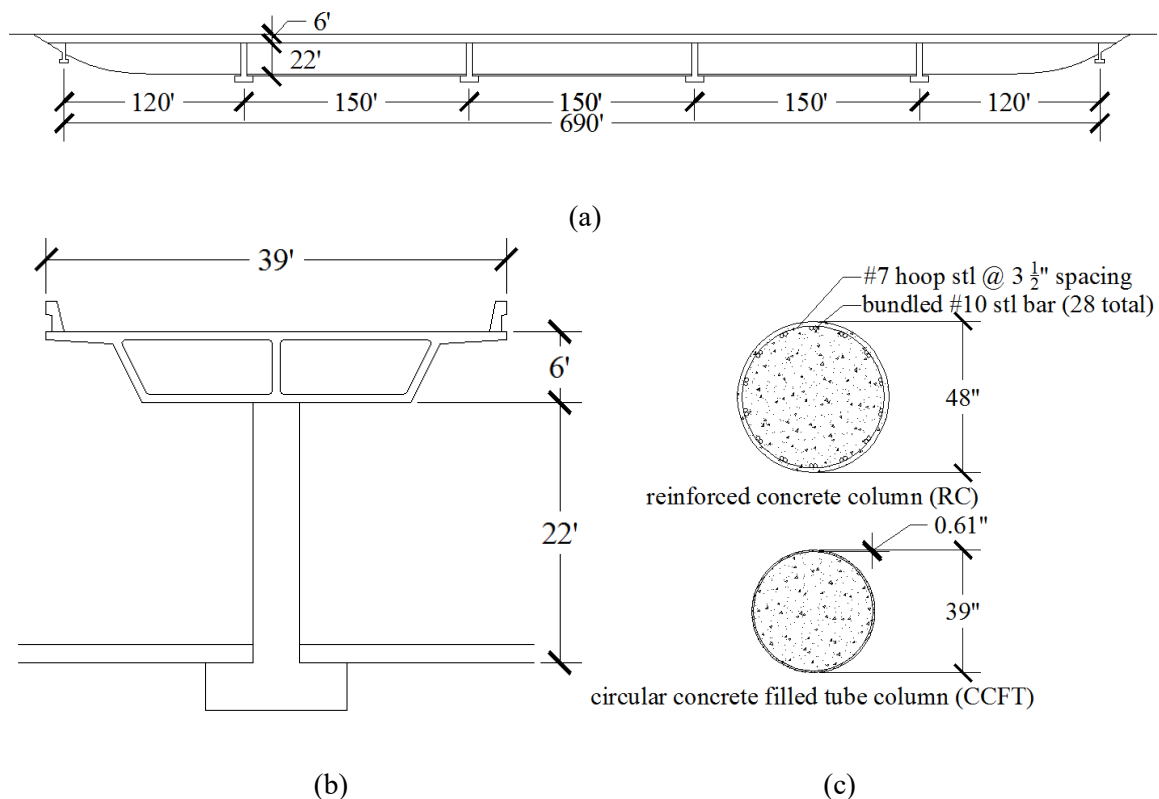
Figure 4.11 Design Basis Bridge: a) Bridge Elevation b) Column Elevation c) RC and CCFT Column Sections

Table 4.1 Design-Basis Bridge RC Column Data (Mackie et al., 2008)

| Input Variable (`name`)	Value (`value, unit`)		Metric Value		Notes
column diameter	48	in.	1.22	m	
column surface area	276	sf	25.68	m²	
number of columns	4	ea	4	ea	
required column casing thickness	0.375	in.	0.0095	m	XS7-010e
column height	22	ft	6.706	m	
bar area	1.27	in.²	0.00082	m²	US #10 bars
diameter of longitudinal bars	1.272	in.	0.0323	m	US #10 bars
number of longitudinal bars	28	ea	28	ea	
percent transverse reinforcement	1.59	%	1.59	%	
percent long. reinforcement	2.0	%	2.0	%	
column dead load (bottom)	1837	k	8171	kN	
col gross area (A_g)	1810	in.²	1.168	m²	
column cover	1.5	in.	0.038	m	
total column bar volume (long.)	5.43	cf	0.154	m³	
total column bar weight (long.)	2662	lb	1207	kg	
steel (f_{ye})	68	ksi	468843	kPa	
concrete (f'_{ce})	5.20	ksi	35853	kPa	
steel weight	490	lb/ft³	76973	N/m³	
concrete weight	150	lb/ft³	23563	N/m³	
steel weight estimate (BDA 11-5)	16.72	lb/ft³	268.0	kg/m³	BDA 11-5
total column gross volume	276.53	ft³	7.826	m³	

4.2 Force-Moment Interaction Diagrams

A CCFT column was designed to match the moment capacity of the original RC column of the design-basis bridge using a relatively large D/t ratio of 64. Steel strength was chosen using AISC's recent adoption of ASTM A1085-13 steel specification for HSS (Winters-Downey et al., 2013). Concrete strength was matched to that of the design basis bridge's RC column.

To determine strength of the proposed CCFT column, a force-moment (P-M) interaction diagram was created using the AISC recommended method for CCFT (Gerschwindner et al., 2010). This involves using plastic section moduli of areas of steel and concrete in radian measure for five points and linearly interpolating between the points as needed. An interaction diagram was created for the design-basis bridge RC column using radian measure and stress block calculations for the concrete and reinforcing steel — see Appendix C for calculations and Maple script used. Additionally for comparison, an HSS of same diameter and tube thickness as the CCFT was included in the interaction diagram.

The calculations used to create the CCFT interaction curve (Gerschwindner et al., 2010, Leon and Hajjar, 2007, 2008) consider combined axial and bending loads. The HSS slenderness ratio, also referred to as the D/t ratio, is still of primary importance. This method is shown in Appendix C.

Figure 4.2 shows a comparative interaction diagram of the CCFT used in this study and that of the corresponding HSS. For comparison purposes, the interaction curve for the HSS component is calculated using a radial stress block method and AISC code equations.
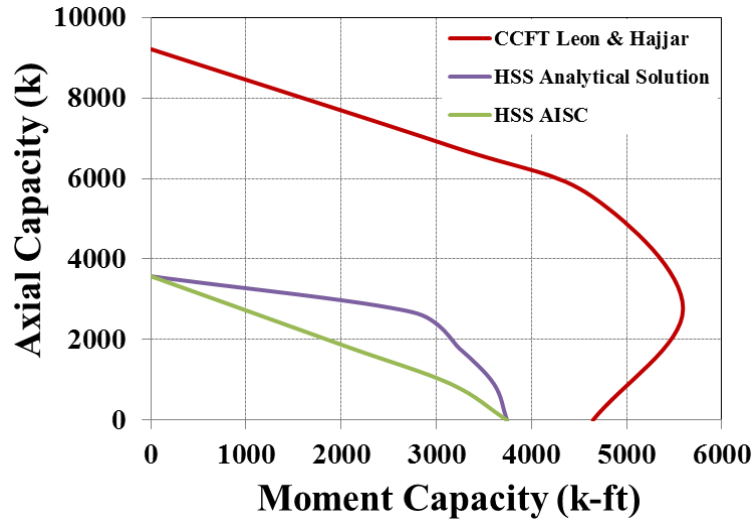
Figure 4.12 Interaction Diagram of CCFT as Compared with HSS

As observed in Figure 4.2, addition of the concrete-filling results is significantly larger in capacity for the CCFT, both axially and in bending, than that for the HSS (about 50 percent greater peak moment capacity). Additionally, the HSS (unfilled) axial capacity of 3,575 kips indicates that for the design basis bridge used for this study and its corresponding gravity load of 1,822 kips, the HSS alone is capable of resisting all of the axial load.

To obtain the equivalent CCFT column, the maximum moment capacity of the RC column was matched using different CCFT column diameters and typical D/t ratios. For a D/t ratio of 64, a 39 in. outer diameter and a 0.61 in. thick steel tube resulted in the closest fit to the peak moment capacity. Using a diameter of 38 or 40 inches would have resulted in a more standard diameter, the differences were significant enough that a 39-inch diameter was selected. Although not technically an HSS or Jumbo HSS —as the size is too large — it is treated as though subject to the same standards set by AISC and ASTM, and uses concrete design strength equal to the RC column of the PEER evaluated design-basis bridge, $f_c' = 5.2$ ksi.

Figure 4.3 shows the P-M interaction diagrams of the bridge RC column at full design strength and the proposed CCFT column as a function of concrete age. The RC column has the greater resistance axially, due in part to its larger cross-sectional area, but the CCFT column has a larger moment resistance because of the steel tube outer perimeter location. Another important advantage of the CCFT column was found in comparing the moment capacity when no axial load is applied to the maximum moment capacity. These two values (4,645 and 5,593 k-ft., respectively) indicate that without axial load, the CCFT has 83% of its maximum moment capacity as compared to the corresponding values of the RC column (3,461 and 5,591 k-ft.), equating to the RC column having only 62% of its maximum moment capacity without axial load being applied.

22
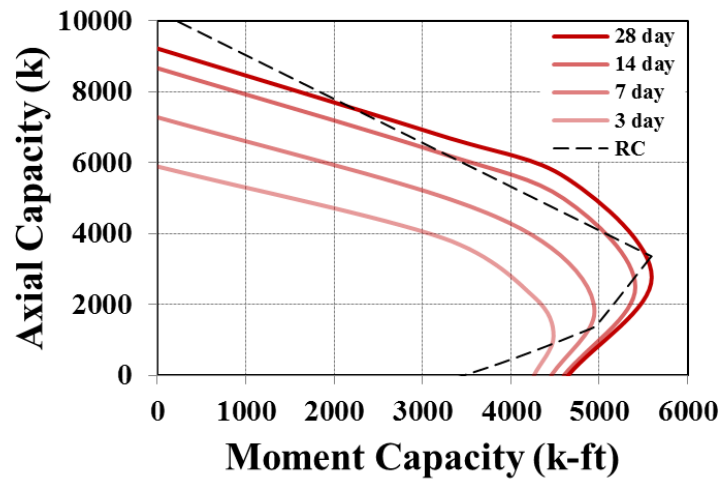
Figure 4.13 CCFT and RC column interaction diagrams as a function of time

Using the largest moment capacity as a reference point, it is observed that the RC column has a larger axial resistance because it has a greater cross section, but the CCFT has the greater moment resistance due to the optimal location of the steel material. To evaluate the effect of time on the strength of the proposed CCFT, full bond strength is assumed regardless of concrete age.

Concrete gains strength as a function of time as cement is hydrated. The process of cement hydration continues for years, but the most appreciable strength gain occurs in the first 28 days. Determination of percentage concrete strength relative to 28-day concrete strength as a function of time involves several assumptions. Curing conditions such as temperature, sealed versus air curing, and cement type affect the relative strength expected at any given time. Experimental reported values for relative strength gain as a function of time vary (Mindess et al., 2003), but in general, concrete at 28 days is on average 1.5 times stronger than at seven days (but this value varies between 1.3 and 1.7) (Hassoun and Al-Manaseer, 2012).

For this research, 28 days was considered as full strength (or as a value of 1), 14, 7, and 3 days were considered as 0.90, 0.65, and 0.40, respectively. The gain in concrete strength as a function of time is shown in Figure 4.4 a. Figure 4.4 b. uses the data of the P-M diagram of Figure 4.3 to show the relative capacity of the CCFT column as a function of concrete age as a percent of the design f_c' (at 28 days). Results are presented for the conditions of pure axial load, pure bending moment, and maximum moment capacity. As observed, the moment capacity of the column is less dependent on time than the axial capacity because the largest contribution to moment capacity is provided by the steel tube.
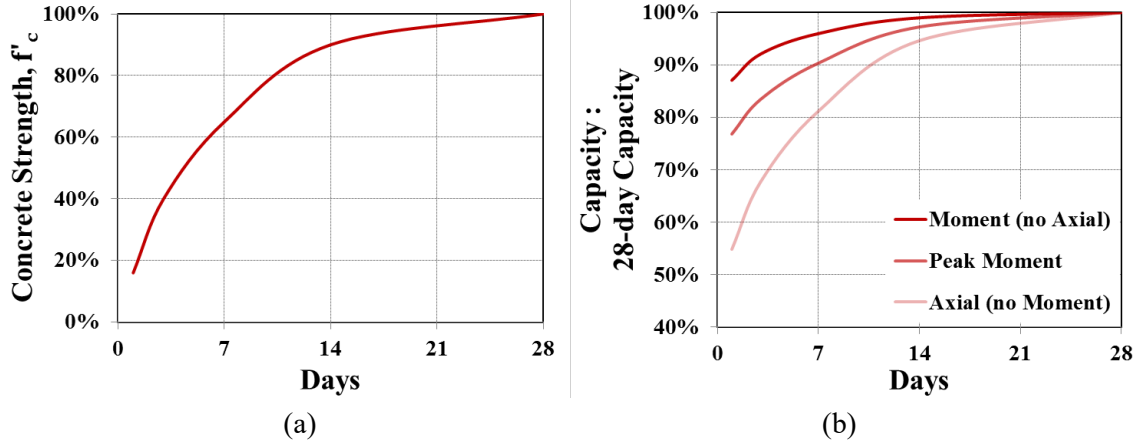
Figure 4.14 a) Concrete Strength as a Function of Time b) Relative capacity of CCFT column as a function of time for moment (no axial), peak moment, and axial (no moment)

Table 4.2 summarizes data for the proposed CCFT. The full data table is in Appendix A. The number at the end of the CCFT acronym refers to curing time. The yield moment of the CCFT specimens, M_y, is determined by inspection of the hysteretic curves (lacking experimental pushover curve data) and compared with the plastic moment of the specimens, M_p, as calculated using AISC P-M diagrams. The resulting ratio of experimental M_p to M_y values is averaged and used to determine the predicted value of M_y for the proposed column. Similarly, from inspection of experimental hysteretic curves, a ratio of M_c to M_y, or the ratio of maximum moment capacity to yield moment capacity, is determined and verified through curve-fitting the analytical hysteretic model to experimental hystereses. This M_c/M_y ratio is then used to predict M_c values for the proposed CCFT as a function of concrete age.

24

Table 4.2 Summary Data for Proposed CCFT as a Function of Time

	CCFT28	CCFT14	CCFT7	CCFT3
D/t	64			
h (in)	264			
A_s/A_c	0.07			
% concrete strength	100%	90%	65%	40%
f'_c (ksi)	5.2	4.68	3.38	2.08
Δ_{AISC} (in)	10.1	10.3	10.8	11.6
Δ_{AASHTO} (in)	12.7	12.8	13.3	14.0
θ (= $P\Delta/Vh$)	0.072	0.073	0.076	0.080
P_y (AISC P_n) (k)	9213	8659	7275	5890
P/P_y	0.19	0.21	0.25	0.30
M_p (AISC) (k-ft)	5258	5180	4943	4345
M_p/M_y	0.87			
M_y (k-ft)	6039	5949	5677	4990
$M_{y,P-\Delta}(M_y(1-\theta))$(k-ft)	5602	5513	5245	4592
M_c/M_y	1.3			
M_c (k-ft)	7851	7734	7380	6487
F_y (= M_y/h) (k)	275	270	258	227
F_y/W	0.12	0.11	0.11	0.10
k (k/in)	94	93	89	85
$T_1(2\pi(m/k)^{1/2})$(sec)	1.4101	1.4188	1.4446	1.4799
T_1(OpenSees)(sec)	1.4097	1.4185	1.4443	1.4795

4.3   Analytical Model

Experimental tests show that CCFT nonlinear performance can be reasonably predicted using concentrated plasticity models. Marson and Bruneau found, for instance, localized rupture of the steel tube and pulverized concrete slightly above the fixed base. A concentrated plasticity model was thereby created in the program OpenSees using the Ibarra et al. peak-oriented hysteretic model (Ibarra et al., 2005, Lignos, 2012).

The column is modeled with an elastic beam-column element, meaning that all inelastic or plastic deformation is accounted for in the spring at the base. This zero-length spring represents a deteriorating peak-oriented hysteretic model (Ibarra et al., 2005, Lignos and Krawinkler, 2012). The OpenSees script allowed for monotonic loading, static cyclic loading using Marson and Bruneau's loading protocol, single dynamic record loading, and IDA. The analysis options could include or disregard P-Δ effects to isolate geometric from material non-linearity. The gravity load lumped at the top node of the elastic beam-column element includes the dead load, as calculated from the superstructure self-weight for the tributary area of the design-basis bridge, as well as the self-weight of the column.

Because all plastic deformation is accounted for in the concentrated hinge location, and the elastic beam-column element has no dimensional width, the elastic beam-column input only needs to have a few definitions provided:

- EI_{eff}, the product of equivalent modulus of elasticity and equivalent moment of inertia;
- h, the column height;
- m, the concentrated mass;
- P, the applied horizontal force;
- M_y, the yield moment capacity; and
- M_c/M_y, the maximum moment capacity to yield moment capacity ratio.

4.3.1 Deterioration Parameters

Deteriorating hysteretic parameters were determined from the experimental data of Marson and Bruneau (2004). These parameters are in large part a function of the stability coefficient, θ, ratio of steel tube diameter to thickness, D/t, and ratio of area of steel to concrete, A_s/A_c. The analytical model accounts for deterioration due to material non-linearity and P-Δ effects (geometric non-linearity). The main parameters used in curve-fitting the analytical model to the experimental columns included a plastic rotation capacity $\theta_p = 0.08$, a post-capping rotational capacity $\theta_{pc} = 0.10$, basic strength deterioration $\Lambda_s = 4.0$, and accelerated reloading stiffness deterioration $\Lambda_a = 1.6$. Note that the value for basic strength deterioration compares favorably with Lignos' finding that $\Lambda_s = 3.0$ (or greater) indicates slow cyclic deterioration, with steel and concrete beam columns with good cyclic performance having $\Lambda_s = 3.0$. Therefore, $\Lambda_s = 4.0$ is indicative of CCFT behaving better under cyclic loading than either steel or concrete alone, which is in agreement with previous studies in which CCFT specimens exhibited higher axial and bending strength than either steel or concrete beam-columns (Ranzi et al., 2013).

Table 4.3 shows the values for the cyclic deterioration determined appropriate for the experimental CCFT specimens. These results are used to select the backbone curve properties and cyclic deterioration parameters for the proposed CCFT column model. Graphic representation of parameters can be seen in .

**Table 4.3** Cyclic Deterioration Parameters for CCFT

Plastic rotational capacity, θ_p	**0.08**
Post-capping rotational capacity, θ_{pc}	**0.1**
Residual strength ratio, M_r	**0.4**
Ultimate rotational capacity, θ_u	**0.4**
Basic strength deterioration, Λ_s	**4.0**
Unloading stiffness deterioration, Λ_k	**2.5**
Accelerated reloading stiffness deterioration, Λ_a	**1.6**
Post-capping strength deterioration, Λ_d	**0.57**

Based on previous parameter studies (Ibarra and Krawinkler, 2005, Lignos and Krawinkler, 2012), a basic strength deterioration parameter, $\Lambda_s = 4.0$, is quite high, indicating relatively little cyclic deterioration (in general, Lignos found that a high value of $\Lambda_s = 3.0$). This is indicative of CCFT's good cyclic performance.

The experimental specimen CFST64, with θ value similar to the proposed CCFT column, was used as the reference case to select the deterioration parameters needed for curve fitting. The same deterioration parameters were used in all four experimental specimens. As observed in Figure 4.5 and Figure 4.6, this resulted in a close fit to the experimental specimens CFST64 and CFST42. For these two columns, the axial load created the rotation of the backbone curve that was expected. For the two other specimens, CFST51 and CFST34, the experimental plots indicate an axial load that does not result in significant P-Δ effects (there is little backbone curve rotation visible), yet the analytical model is anticipating a large θ value based on the reported experimental input. The use of the θ values reported in the experiment for CFST34 and CFST51 ($\theta = 0.15$ and 0.16, respectively) leads to larger backbone curve rotations than those recorded from the tests (Figure 4.7 and Figure 4.9). To create a more accurate curve fit for these two cases, specimens were modeled with a lower axial load (Figure 4.8 and Figure 4.10) resulting in a lower stability coefficient ($\theta = 0.03$ was used in both cases) in accordance with the small P-Δ effects shown in the experimental hystereses. For all figures, the underlying experimental data shown is from Marson and Bruneau (2004).
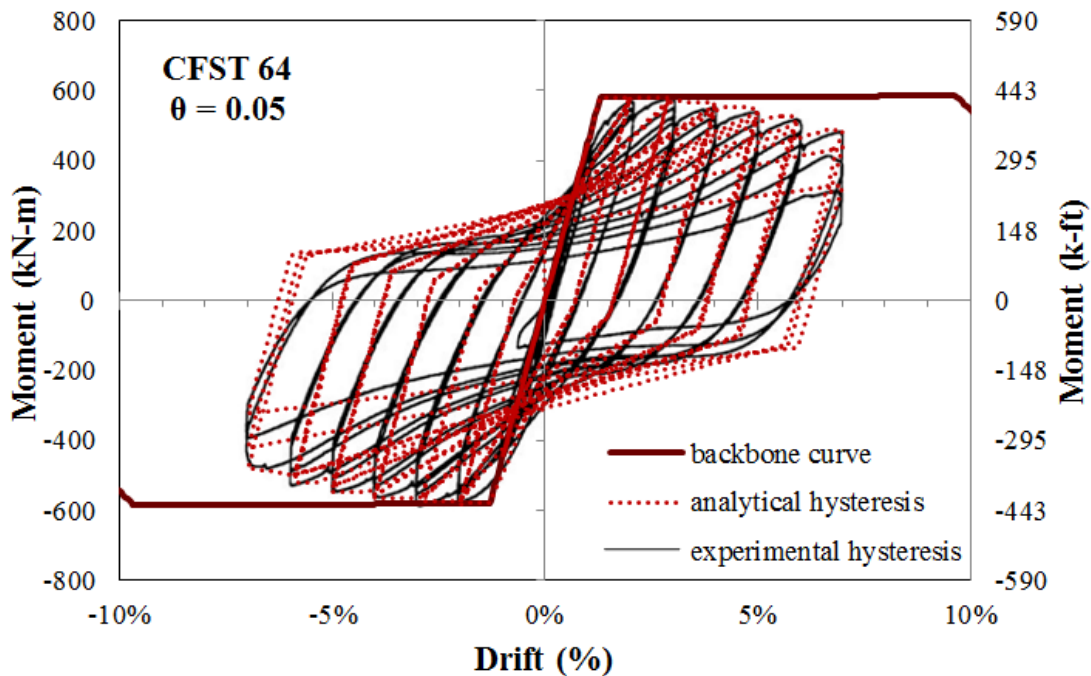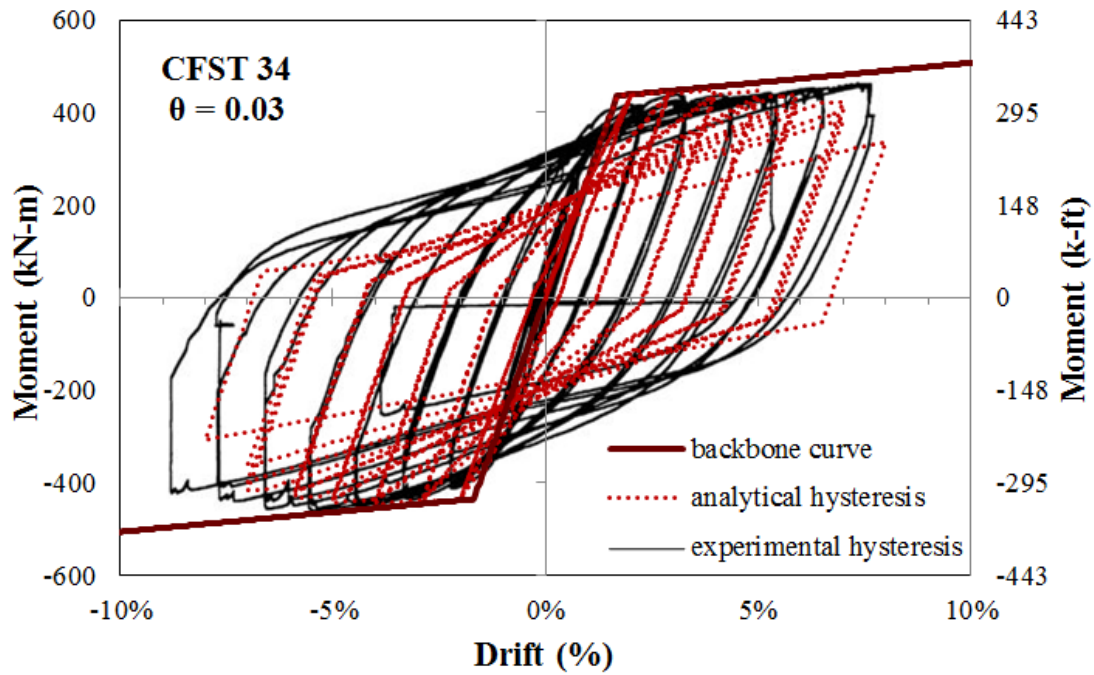

Figure 4.15 CFST64 Experimental and Predicted Analytical Hysteretic Behavior (under Static Cyclic Loading) and Monotonic Backbone Curve
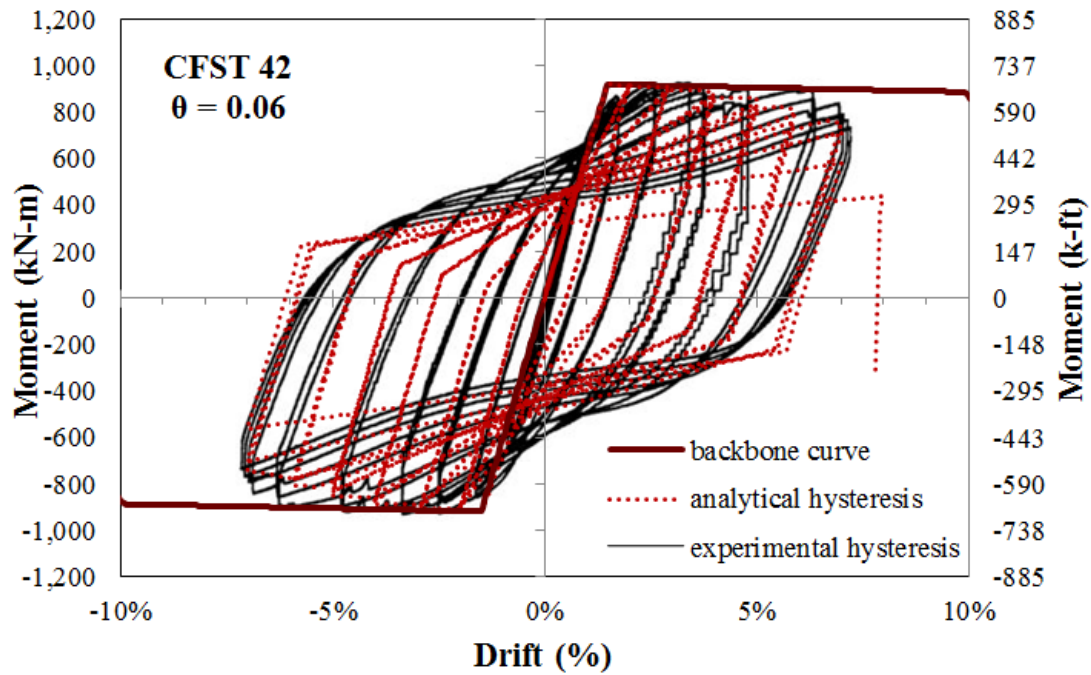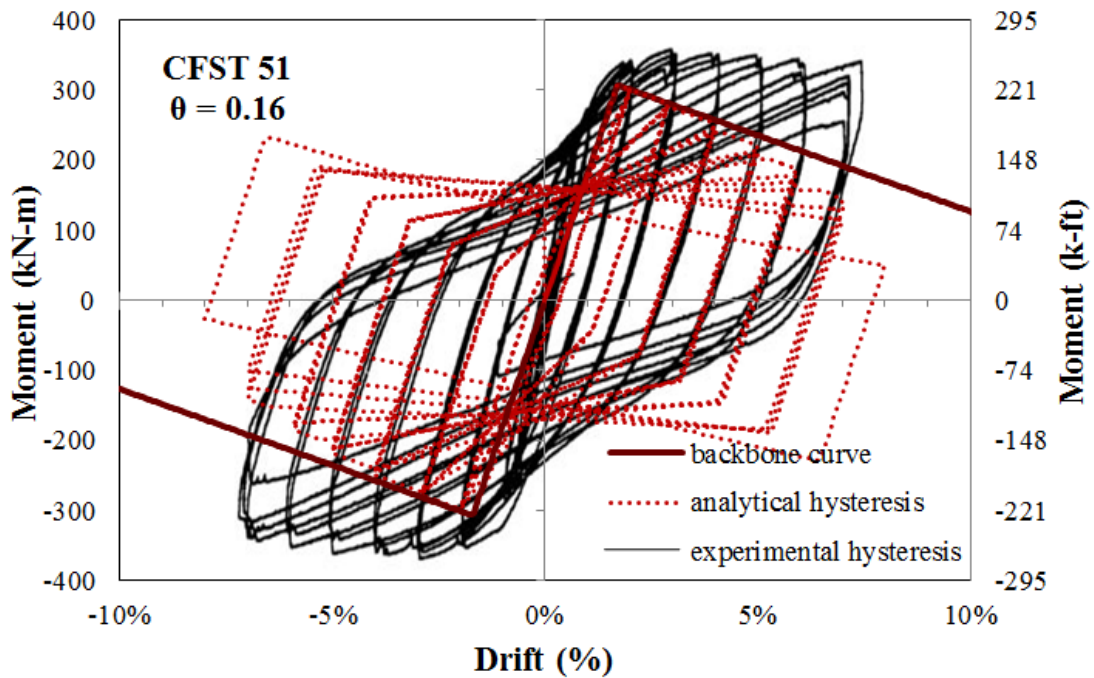
Figure 4.16 CFST42 Experimental and Predicted Analytical Hysteretic Behavior (under Static Cyclic Loading) and Monotonic Backbone Curve
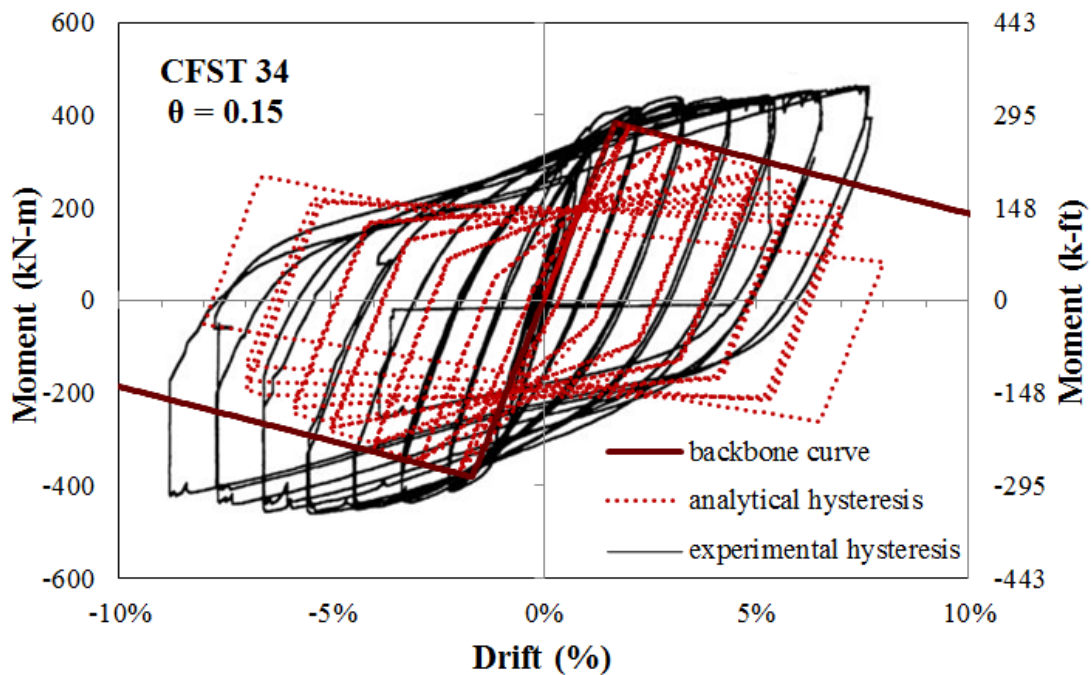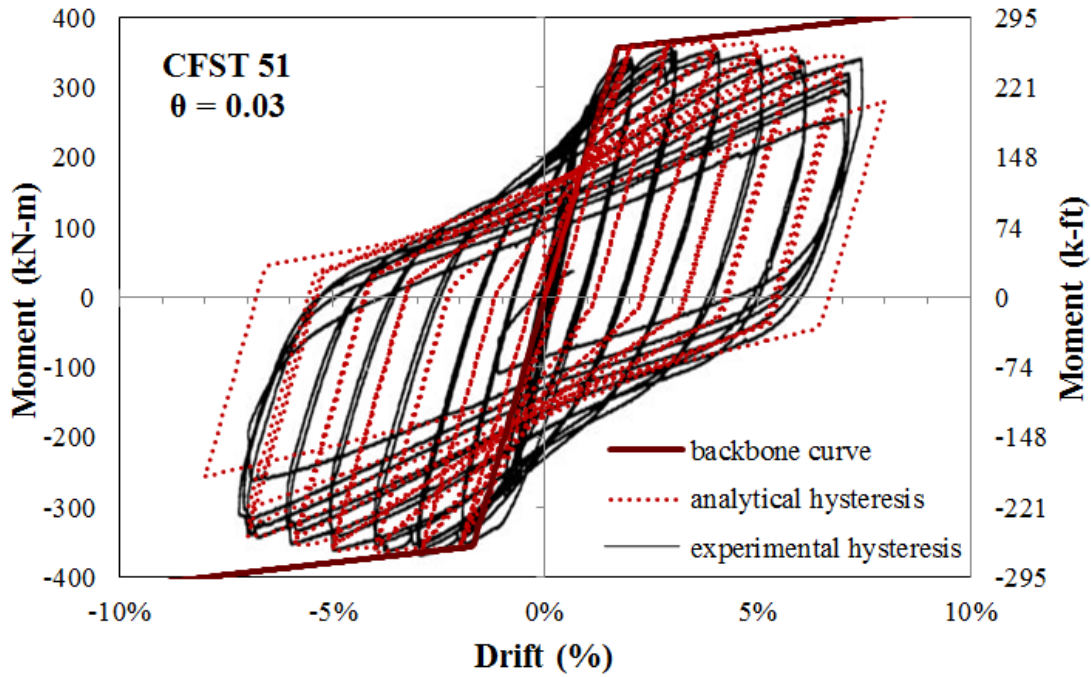

Figure 4.17 CFST34 Experimental and Predicted Analytical Hysteretic Behavior (under Static Cyclic Loading) and Monotonic Backbone Curve, θ = 0.15

Figure 4.18 CFST34 Experimental and Predicted Analytical Hysteretic Behavior (under Static Cyclic Loading) and Monotonic Backbone Curve, θ = 0.03

Figure 4.19 CFST51 Experimental and Predicted Analytical Hysteretic Behavior (under Static Cyclic Loading) and Monotonic Backbone Curve, θ = 0.16

Figure 4.20 CFST51 Experimental and Predicted Analytical Hysteretic Behavior (under Static Cyclic Loading) and Monotonic Backbone Curve, $\theta = 0.03$

4.4   Analytical Hysteretic Model Results

Figures 4.11–4.14 show the effects of gain in concrete compressive strength on the hysteretic response of the deteriorating CCFT column as a function of several concrete ages. As observed, CCFT column performance after three days is almost 80 percent of that of the CCFT at 28 days. By 14 days, the behavior is virtually identical with that expected of full design-strength concrete. Where the upper limit of response is indicated by the backbone curve, the relatively small decrease seen in the cyclic behavior, in all cases of concrete age, is indicative of the good ductility of the CCFT column.
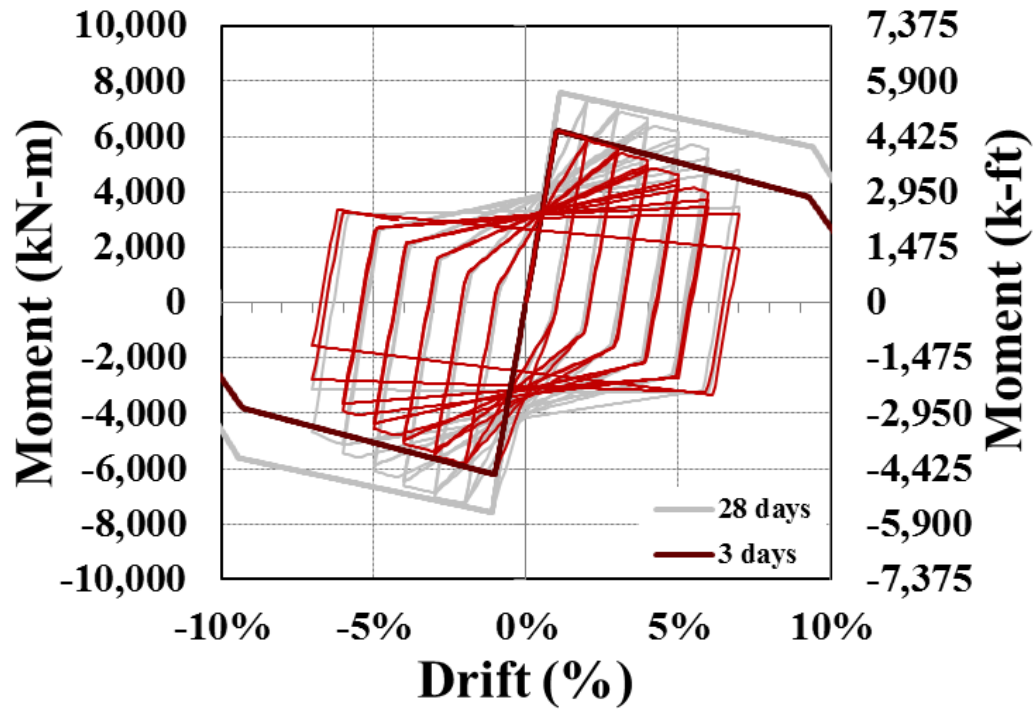
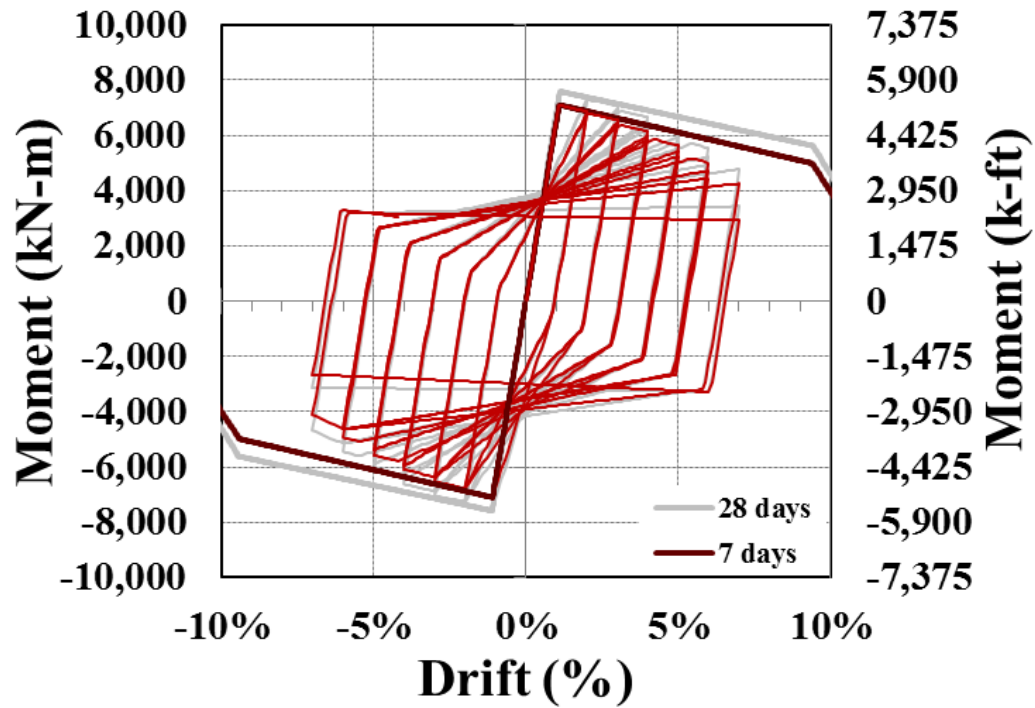**Figure 4.21** Hysteresis of Proposed CCFT at three and at 28 Days

Figure 4.22 Hysteresis of Proposed CCFT at seven and at 28 Days
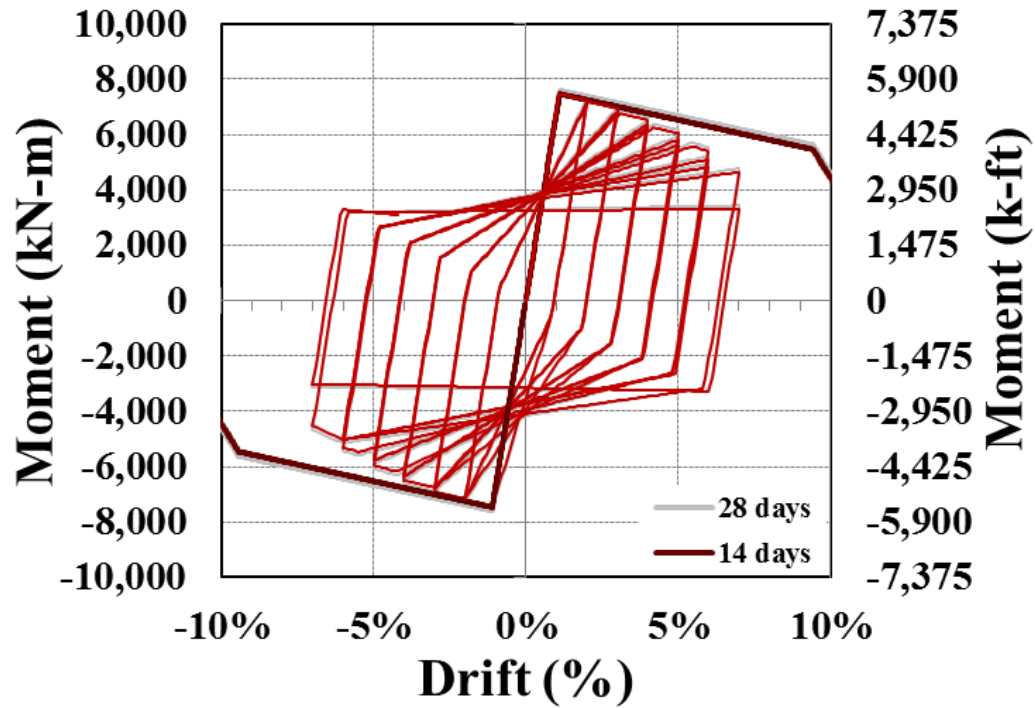
31

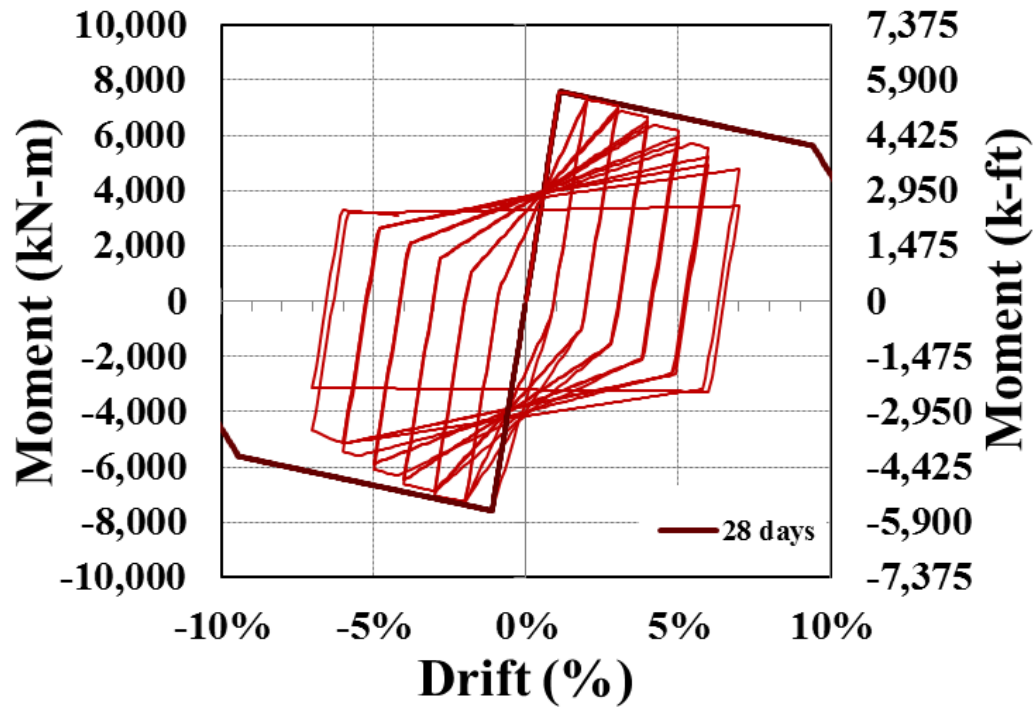**Figure 4.23** Hysteresis of Proposed CCFT at 14 and at 28 Days

Figure 4.24 Hysteresis of Proposed CCFT at 28 Days

4.5   Incremental Dynamic Analysis

Incremental dynamic analyses (IDAs) were performed using FEMA P695 set of 44 far-field ground motion records (ATC, 2009) using an OpenSees script from Vamvatsikos (2011, 2004). The records were scaled at the 5 percent-damped spectral acceleration of the fundamental period of the system (S_a/g). Figures 4.15–4.18 show individual and statistical IDA curves as a function of CCFT concrete age. As the overall capacity increases with time, so does the dispersion of the IDAs. Note that most of the CCFT capacity is due to energy dissipation in the nonlinear range — the IDA becomes nonlinear at approximately $\theta = 0.5\%$.
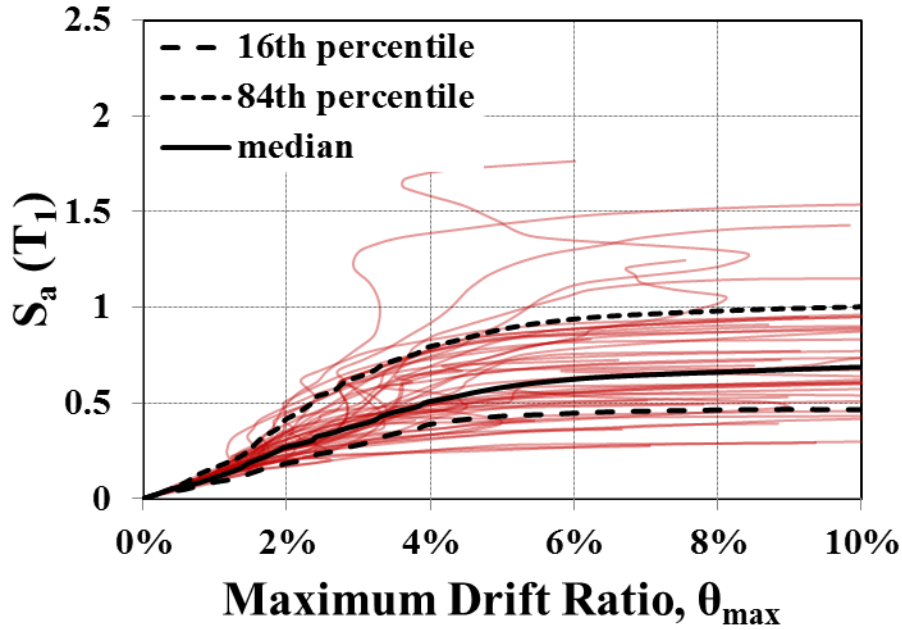

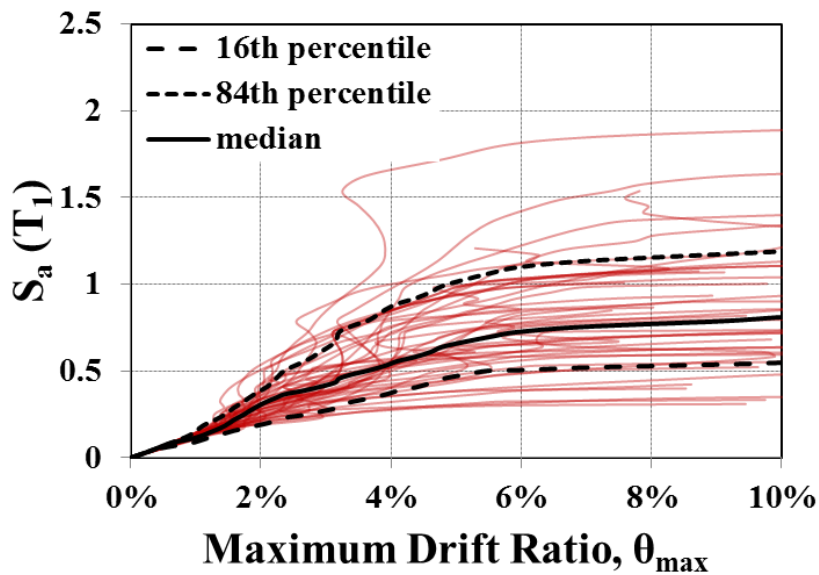**Figure 4.25** Incremental Dynamic Analysis of Proposed CCFT at 3 Days

Figure 4.26 Incremental Dynamic Analysis of Proposed CCFT at 7 Days
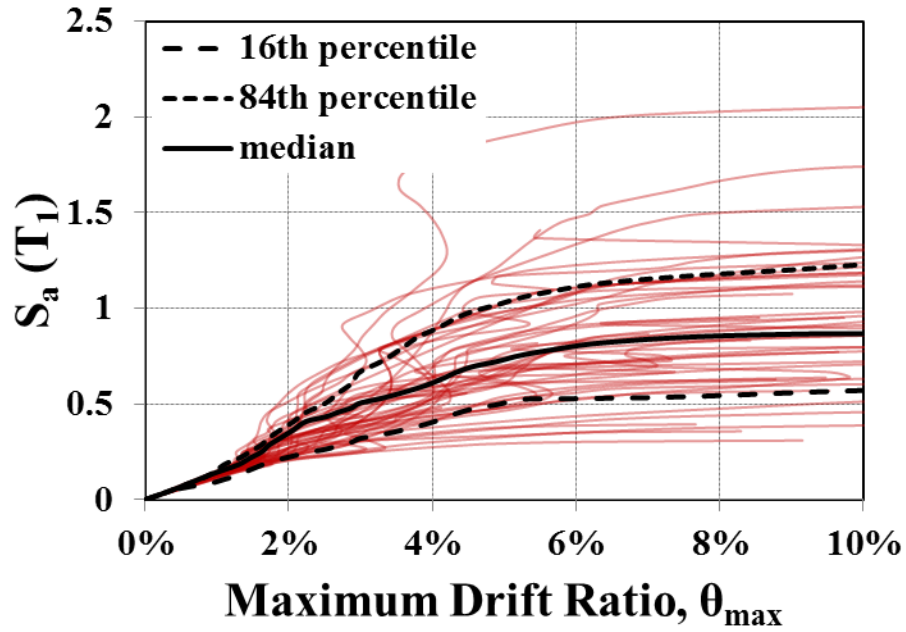
33

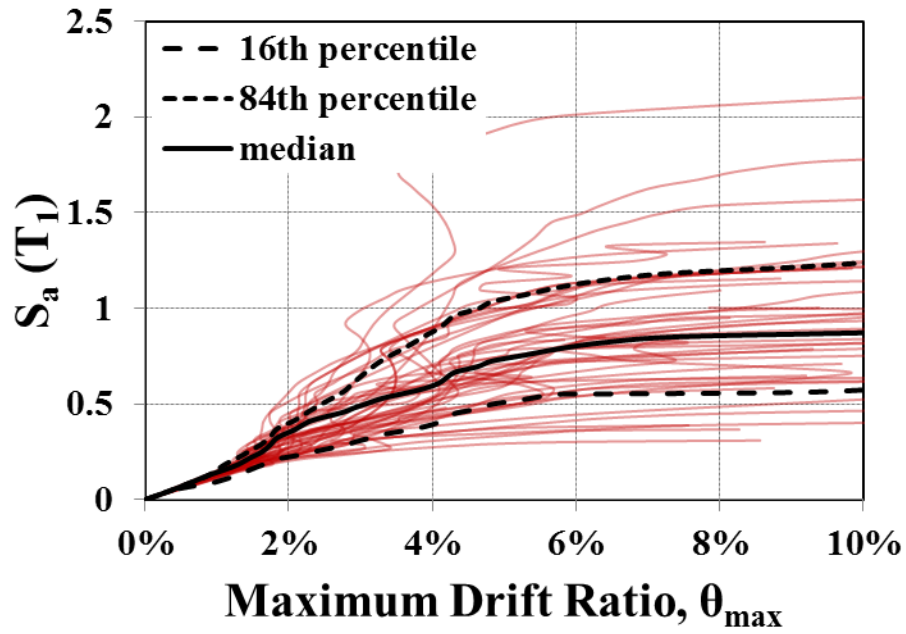**Figure 4.27** Incremental Dynamic Analysis of Proposed CCFT at 14 Days

Figure 4.28 Incremental Dynamic Analysis of Proposed CCFT at 28 Days

Figure 4.19 compares median IDAs as a function of concrete age. The point at which the IDA becomes nonlinear corresponds to the ratio of the system's effective yield strength to its effective seismic weight, F_y/W. Increasing concrete age is incorporated into the model through the product of modulus of elasticity and moment of inertia, EI_{eff}. As EI_{eff} increases, F_y/W likewise increases. Differing values for F_y/W are reflected in the lack of agreement on the point at which nonlinearity should begin. This similarly reflects θ and T_1 being slightly different for the CCFT as a function of time: T_1 and θ both increase as EI_{eff} decreases. In other words, period elongation at lower EI_{eff} values is advantageous, but the associated increase in drift is an area for concern. However, as is shown in the probabilistic analysis, even at three days, the performance under the resulting drift ratios is sufficient.
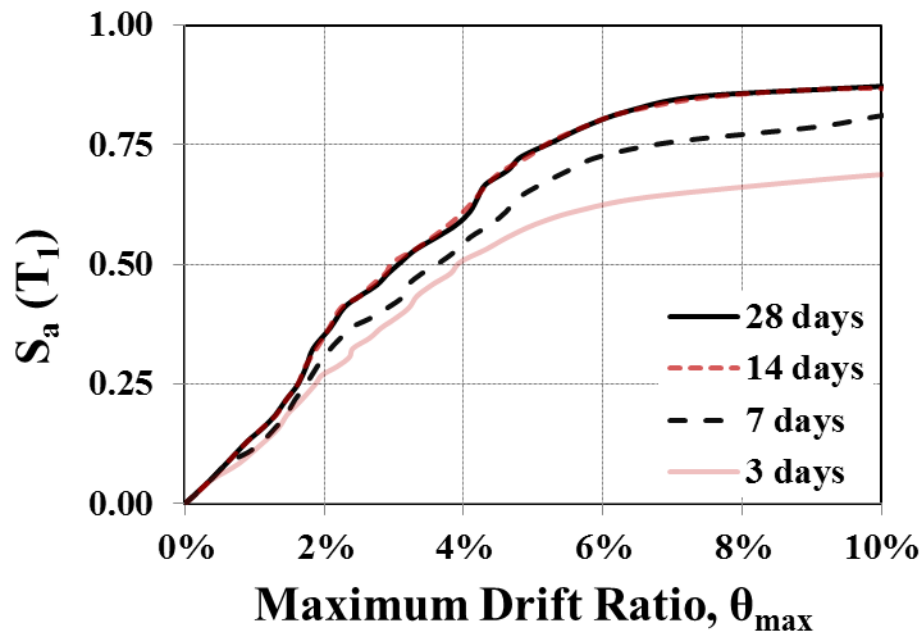
Figure 4.29 Median IDAs as a Function of Time

The comparative results of the median IDA values show that the dynamic behavior of the column at 14 days is practically the same as expected for the full-capacity column at 28 days. Of central importance is that considering the value of F_y/W at, for example, 28 days, is 0.12, the energy dissipated by the CCFT is largely in the non-linear range.

Furthermore, the column's capacity (the drift capacity prior to collapse) after three days is already about 80 percent of the full-capacity column. Additionally, the calculated static drift ratio for the CCFT column compares well with that of the original design basis bridge RC column. At 3, 7, 14, and 28 days, the CCFT column has a static drift ratio (AASHTO, 2012) of 4.4%, 4.1%, 3.9%, and 3.8%, respectively, as compared with the original design basis bridge RC column's drift ratio (ACI, 2008) of 3.3%.

4.6   Effect of P-Δ on CCFT behavior

The stability coefficient, Equation (10), can be interpreted as the amount the backbone curve rotates when geometric nonlinearities (P-Δ effects) are included. Whether or not geometric nonlinearities are considered, the modeling done for this research includes effects of material nonlinearity, although the P-Δ effect is not obtained by rotating the SDOF model, but by inputting the parameters that control θ. Figures 4.20 and 4.21 show the behavior under the monotonic and quasi-static cyclic loading conditions for the CCFT at 28 days, with and without P-Δ effects.

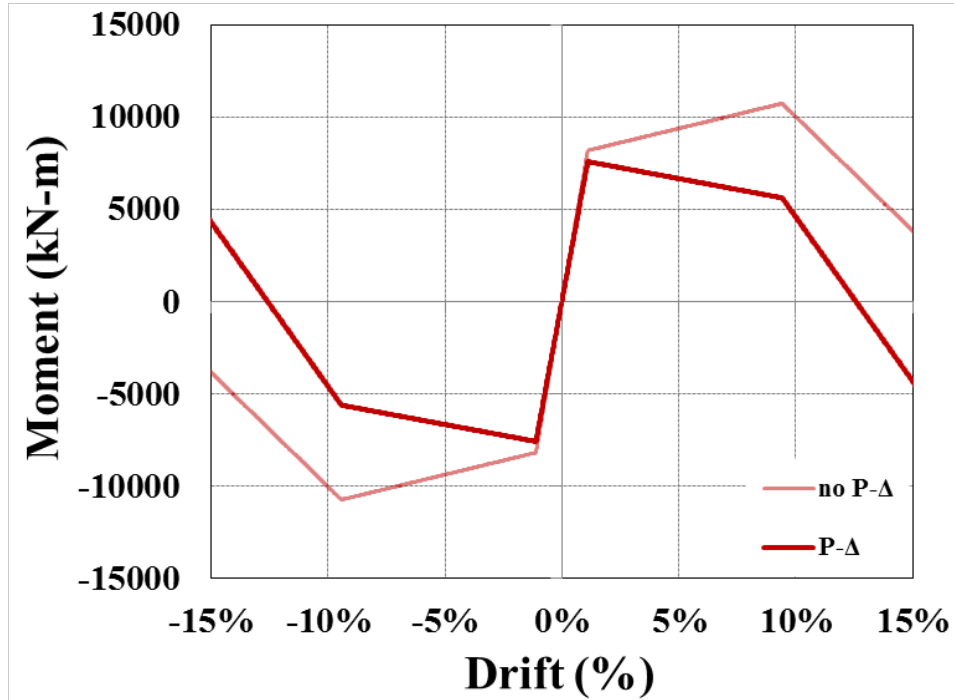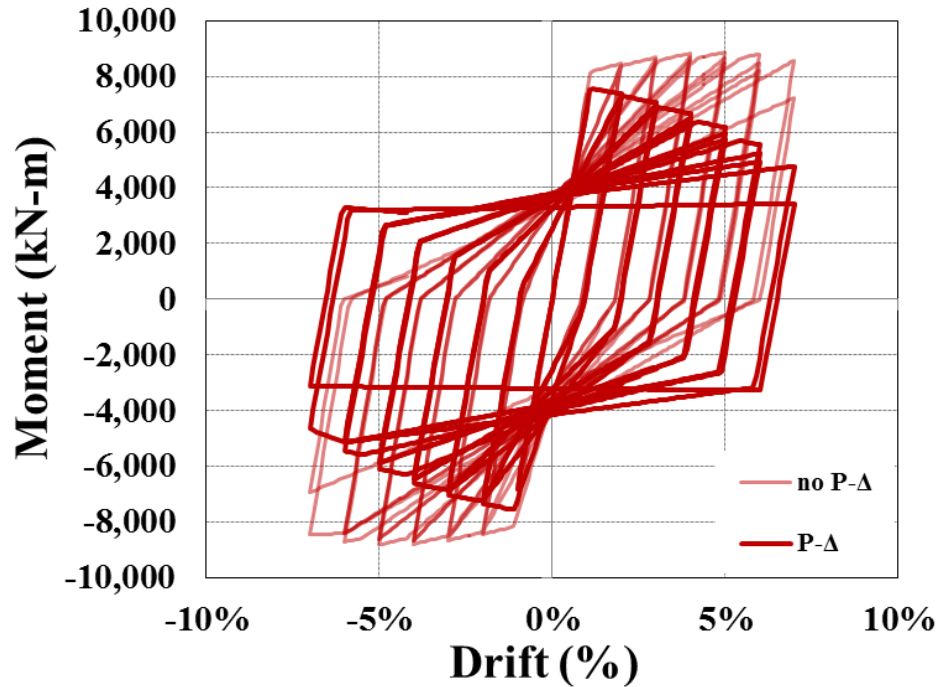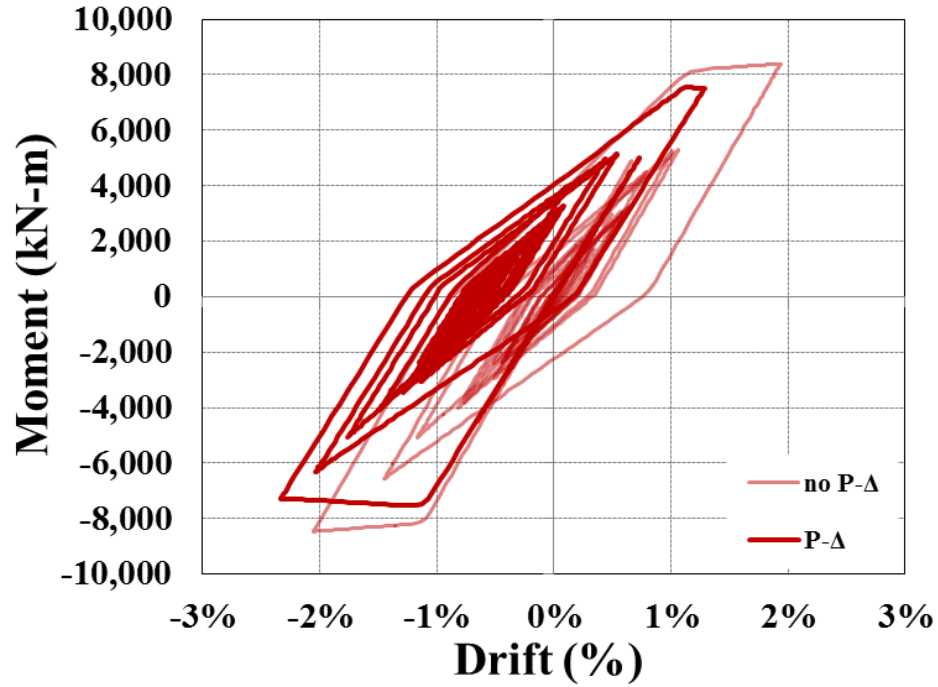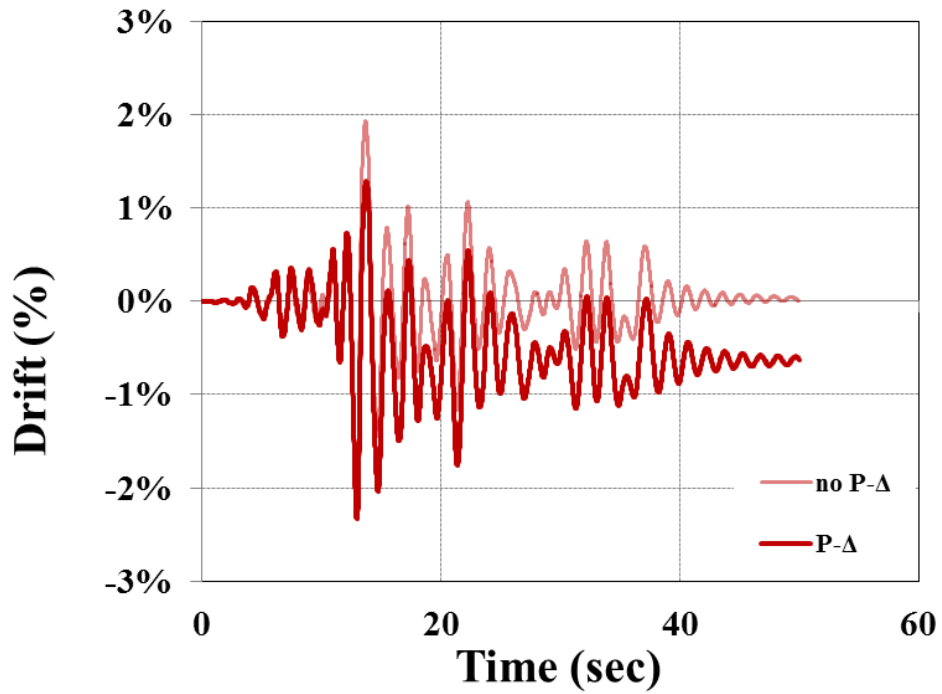**Figure 4.30** Backbone Curve of Proposed CCFT at 28 Days with and without P-Δ

Figure 4.31 Quasi-Static Cyclic Loading (Peak-oriented Hysteretic Curve) of Proposed CCFT at 28 Days with and without P-Δ

Figure 4.20 shows comparative drift versus bending moment, or the pushover curves, with and without P-Δ effects. The yielding moment, where the CCFT becomes nonlinear, occured at approximately 1.2% drift, or 0.07 meters of lateral displacement. The peak strength, at approximately 9.5% drift, was equivalent to 0.64 meters of lateral displacement. This is as compared with allowable lateral deflections under AISC and AASHTO of 0.26 meters and 0.32 meters, respectively (around 4-5% drift). The quasi-static cyclic behavior is shown in Figure 4.21. The same rotation as in the pushover curve, due to P-Δ effects, can be seen.

P-Δ effects on CCFT behavior are presented below for the 1987 Superstition Hills ground motion record (SUPERST/B-ICC000). The record was selected because its IDA closely matched the median IDA response. Figure 4.22 shows the dynamic behavior resulting from the unscaled GM. Figure 4.23 shows the resulting drift as a function of time. For this particular GM, the CCFT's peak drifts, with and without P-Δ effects, were 2.3% and 2.1%, respectively. The residual drift considering P-Δ effects was 0.6%. Without P-Δ effects, there was no residual drift. Figure 4.24 shows dynamic behavior resulting from the unscaled GM. Figure 4.25 shows the resulting drift as a function of time. For this particular GM, the CCFT's peak drifts, with and without P-Δ effects, were 6.6% and 5.4%, respectively. The corresponding residual drifts were 5.6% and 1.8%. For this case, P-Δ had a small effect on the maximum response, but significantly increased residual drifts.
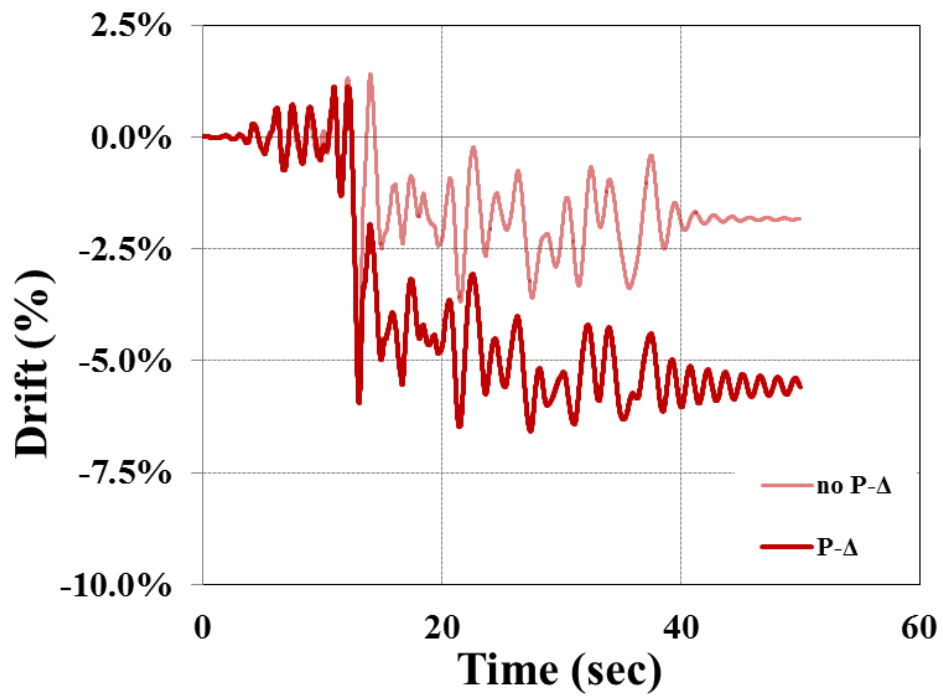
Figure 4.32 Dynamic Loading (Peak-oriented Hysteretic Curve) of Proposed CCFT at 28 Days with and without P-Δ (unscaled GM)

Figure 4.33 Dynamic Loading (Peak-oriented Hysteretic Curve) of Proposed CCFT at 28 Days with and without P-Δ (unscaled GM)
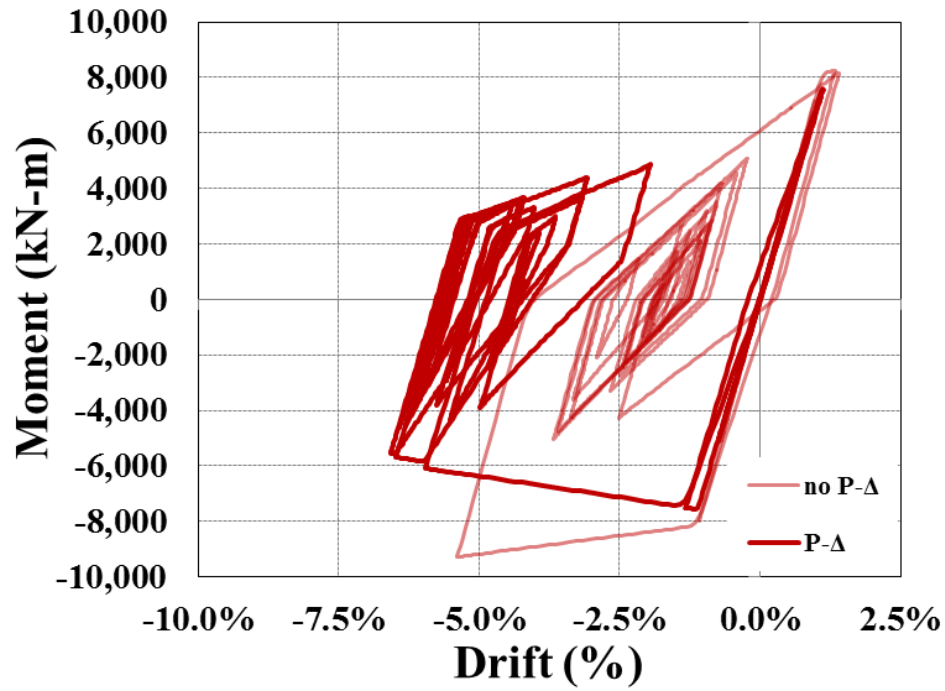
Figure 4.34 Dynamic Loading (Peak-oriented Hysteretic Curve) of Proposed CCFT at 28 Days with and without P-Δ (GM scaled to 2)


Figure 4.35 Dynamic Loading (Peak-oriented Hysteretic Curve) of Proposed CCFT at 28 Days with and without P-Δ (GM scaled to 2)

Figure 4.26 shows comparative IDAs, with and without P-Δ effects. Of interest is that until roughly 5% drift, the IDA results were similar, whether or not P-Δ is considered as part of the analysis. However, at drifts larger than 5%, the difference was increasingly important.
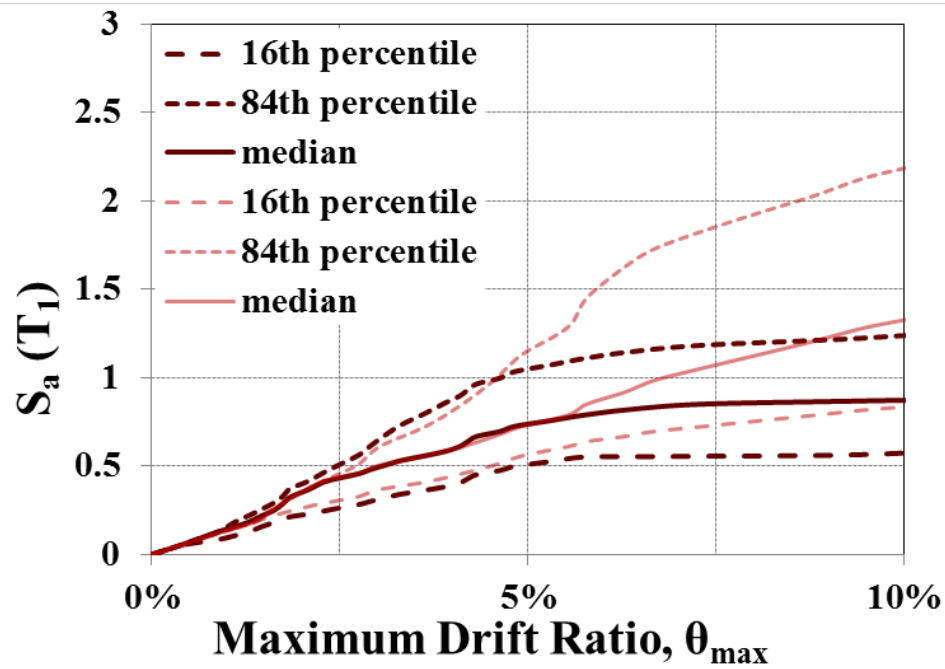
Figure 4.36 Incremental Dynamic Analysis, Using 44 GMs, of Proposed CCFT at 28 days with and without P-Δ

5. EFFECT OF TEMPORARY CONDITIONS ON CIRCULAR CONCRETE-FILLED STEEL TUBE COLUMNS' SEISMIC PERFORMANCE

The time required for the column's concrete to meet the design compressive strength creates a temporal condition if the bridge is open to traffic before 28 days. The ultimate goal of this study was to estimate the seismic probability of failure for this temporary condition. The alternatives for developing seismic criteria for temporary conditions include i) the use of standard seismic loads with a relaxed acceptance criteria, or ii) reduction of seismic loads with a standard design criteria (Amin et al., 1999).

A reduced seismic load (RSL) can be achieved by several approaches that are controversial due to the illogical implications for temporary conditions that may arise from arbitrarily discretizing a permanent condition, and the inability to provide constant failure or fatality frequencies. In the case of CCFT columns, temporal conditions are clearly defined (i.e., the days the concrete must reach the design compressive strength), and arbitrary discretizations of time can be excluded. Thus, RSLs are obtained following the approach presented by Amin et al. (Amin et al., 1999, Amin and Jacques, 1994) in which:

$$RSL = k \cdot DBSL \qquad (15)$$

Where $DBSL$ is the design basis seismic load, and k is a reduction factor that depends on duration of the temporary condition. In this study, it is conservatively assumed that $k = 1/12$ (representing about one month) for the three temporary conditions at 3, 7, and 14 days.

Regarding the system's capacity, for the CCFT at 28 days (Figure 4.19), median collapse capacity was $\overline{m}_{S_a} = 0.88$ g, and the standard deviation of the log of the collapse capacity $\beta = \sigma_{lnS_a} = 0.420$. This dispersion on collapse capacity due to RTR variability was practically the same for CCFT columns with concrete cured for 7 and 14 days. For CCFT at 3 days, the dispersion was slightly higher ($\beta = 0.422$).

The mean annual frequency of collapse (λ_{CC}) can be expressed as the mean annual frequency of the strong motion intensity (S_a) being larger than the collapse capacity (i.e., λ_{S_a}), multiplied by the probability of having such a strong motion intensity (i.e., $F_{C,S_{a,c}}(x)$),

$$\lambda_{CC} = \int_0^\infty F_{C,S_{a,c}}(x) . \left| d\lambda_{S_a} \right| \qquad (16)$$

The above equation was solved by numerical integration for the four CCFT columns to determine the probability of failure.

Figure 5.1 shows the mean hazard curve (λ_{S_a}) assuming the bridge is located in Salt Lake City, Utah, and the reduced hazard curve for evaluation of temporary conditions presents the fragility curves of the CCFT columns, $F_{C,S_{a,c}}(x)$, at the collapse capacity limit state that was used to obtain the probability of failure. The numerical integration of the RSL hazard curve and the CCFT columns at 3, 7, and 14 days, resulted in the values for P_f as a function of time listed in Table 5. Those values in bold text are the P_f values proposed for use in this study.
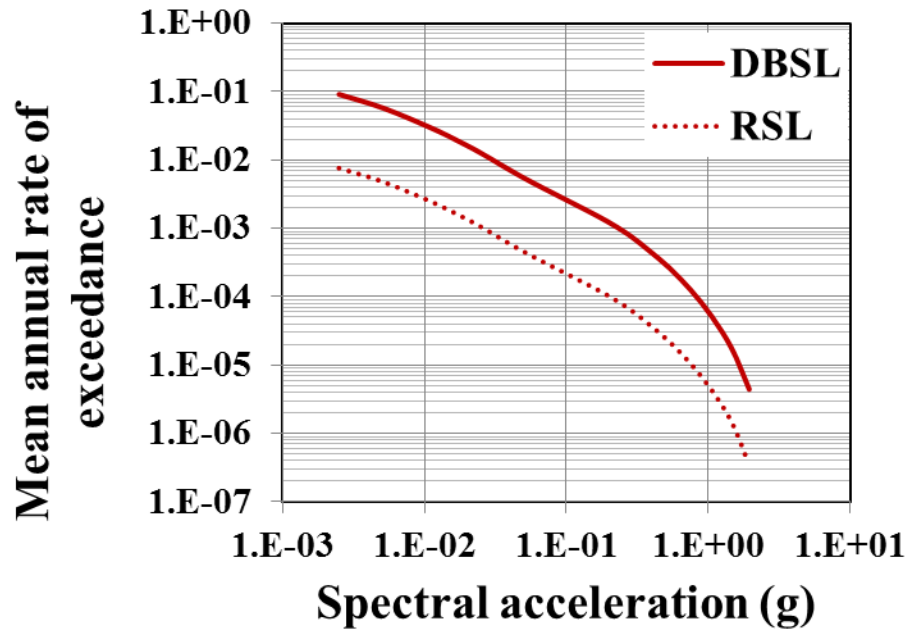
Figure 5.37 Hazard Curve for Salt Lake City, UT for T_1=1.40 s. for DBSL and RSL conditions
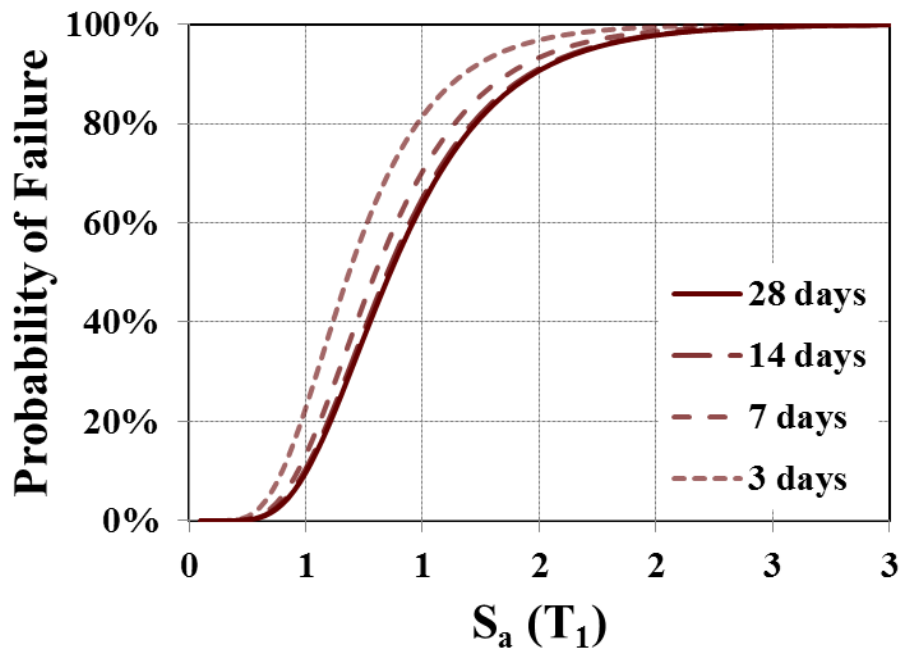

Figure 5.38 Fragility curves for the four CCFT evaluated conditions

42

Table 5.1 CCFT Probability of Failure as a Function of Time

| | mean annual P_f for 75 years: | | |
Days	$k = 1$	$k = 1/12$	$k = 1/2$
28	**1.32E-04**	1.10E-05	6.62E-05
14	1.37E-04	**1.14E-05**	6.86E-05
7	1.56E-04	**1.30E-05**	7.80E-05
3	2.13E-04	**1.77E-05**	1.06E-04

For the CCFT column at 28 days and the original hazard curve, the computed probability of failure, P_f, was $P_f = 1.32 \times 10^{-4}$. The proposed values for P_f for one month (using $k = 1/12$ for 14, 7, and 3 days) were significantly lower than that of the design CCFT column ($P_f = 1.32 \times 10^{-4}$), indicating that the capacity reduction of CCFT columns at 3, 7, and 14 days was compensated by assuming a temporary condition.

Note that the hazard curve reduction factor could have been assumed as $k = 1/2$ (i.e., a temporary condition of six months), and the critical CCFT at three days would render a $P_f = 1.1 \times 10^{-4}$, still lower than the probability of failure for the base case. This conservative calculation implies that the temporary condition could last for six months, instead of three days, and the probability of failure would not exceed that of the base case.

6. CONCLUSIONS

This study assessed the effect of partial concrete compressive strength on the seismic performance of CCFT bridge columns prior to full concrete compressive strength being achieved. If the bridge needs to be open to traffic after a few days, the time required for the columns' concrete to meet the design compressive strength creates a temporary condition. The research evaluated whether this temporary condition increases the seismic probability of failure using as the criterion a comparison of CCFT columns under permanent conditions subjected to DBSL with that of temporary conditions subjected to RSL.

The first phase of the study addressed design of CCFT columns. These components may require one-third less cross-sectional area than the original RC columns to achieve similar capacity under combined axial and bending forces. Because of the highly localized failure mode of CCFT columns, concentrated plasticity models can reliably predict the nonlinear performance of these components up to the collapse limit state. This study calibrates for first time the deteriorating nonlinear parameters required for these numerical simulations.

The gain in concrete strength is not as critical for CCFT columns as in RC columns. Concrete only reaches about 40 percent of its design strength after three days, where the CCFT column achieves 92 percent and 68 percent of its full pure moment capacity and full pure axial capacity, respectively, on day three. Thus, the steel tube is largely responsible for initial capacity of the CCFT, as long as the concrete provides lateral constraint preventing buckling failure.

Based on the incremental dynamic analysis (IDA) analysis, the collapse capacity of CCFT columns at 3, 7, and 14 days correspond to 80, 93, and 98 percent of the CCFT collapse capacity at 28 days, when the concrete is expected to reach its design compressive strength. If a conservative temporary condition of one month is assumed for CCFT columns with less than one month of curing, the probability of failure for CCFT columns at 3, 7, and 14 days is about one order of magnitude smaller than that for the CCFT column over the lifespan of 75 years.

7. RECOMMENDATIONS FOR FUTURE RESEARCH

7.1 Experimental Testing

Two areas of underrepresented experimental research on CCFT were applicable to this project. For research applicable to highway bridges, the current experimental data is missing sufficient number of normal strength concrete/normal strength steel experiments performed with appropriate diameter/steel tube thickness (D/t) ratio and height/diameter ratio. In addition, experimental testing must include specimens tested under monotonic loading for the creation of backbone curves.

7.2 Bond Strength as a Function of Concrete Age

Were experiments to be conducted, it would be of particular applicability to the current research to subject multiple identical specimens to the same loading protocol at various points in the concrete curing time — likely at 3, 7, 14, as well as 28 days. The objective would be to determine seismic performance of the CCFTs as a function of time, and additionally, to determine the relation of concrete curing time to the bond strength between the concrete core and the steel tube.

7.3 Parameter Study for Hysteretic Modeling of CCFT

Nonlinear deteriorating hysteretic parameters were found for modeling of CCFTs of interest. However, these parameters will change depending on the stability coefficient, θ; the diameter to thickness ratio, D/t; and the ratio of area of steel to area of concrete, A_s/A_c. Potential future research could determine specifically which factors have the greatest influence and corresponding ranges of the plastic spring parameters.

REFERENCES

AASHTO, AASHTO LRFD Bridge Design Specifications. Americal Association of State Highway and Transportation Officials: Washington, D.C., 2012.

ACI, Building Code Requirements for Structural Concrete (ACI 318-08) and Commentary. American Concrete Institute: 2008.

Adam, C.; Ibarra, L. F.; Krawinkler, H. In *Evaluation of P-delta effects in non-deteriorating MDOF structures from equivalent SDOF systems*, Proceedings of the 13th World Conference on Earthquake Engineering, 2004.

AISC, Seismic Provisions for Structural Steel Buildings. American Institute of Steel Construction: 2010a.

AISC, Steel Construction Manual. American Institute of Steel Construction: 2010b.

Amin, M.; Budnitz, R. J.; Cornell, C. A.; Kennedy, R. P.; Olson, D. E.; Tang, H. T., Reduced Seismic Loads for Temporary Conditions. *Nuclear Engineering and Design* **1999,** *192*, 167-178.

Amin, M.; Jacques, L. V., Seismic Loading for Evaluation of Temporary Conditions in Nuclear Power Plants. In *Fifth U.S. National Conference on Earthquake Engineering*, Chicago, Illinois, 1994.

An, Y.-F.; Han, L.-H.; Zhao, X.-L., Behaviour and design calculations on very slender thin-walled CFST columns. *Thin-Walled Structures* **2012,** *53*, 161-175.

ATC *Recommended Seismic Design Criteria for New Steel Moment-Frame Buildings, Report No. FEMA 350*; Federal Emergency Management Agency, Washington, DC: 2000a.

ATC *Recommended Seismic Evaluation and Upgrade Criteria for Welded Steel Moment Frame Buildings, Report No. FEMA 351*; Federal Emergency Management Agency, Washington, DC: 2000b.

ATC *Quantification of Building Seismic Performance Factors*; Applied Technology Council: Washington D.C., 2009.

Bernal, D., Amplification factors for inelastic dynamic p–Δ effects in earthquake analysis. *Earthquake engineering & structural dynamics* **1987,** *15* (5), 635-651.

Boggs, D. W.; Peterka, J. A., Wind Speeds for Design of Temporary Structures. In *10th ASCE Structures Congress*, Structures Congress '92 Compact Papers: San Antonio, Texas, 1992.

Boyd, P. F.; Cofer, W. F.; Mclean, D. I., Seismic performance of steel-encased concrete columns under flexural loading. *ACI Structural Journal* **1995,** *92* (3).

Clough, R.; Johnston, S. In *Effect of stiffness degradation on earthquake ductility requirements*, Japan Earthquake Engineering Symposium, Tokyo, Japan, Tokyo, Japan, 1966.

Cornell, C. A.; Bandyopadhyay, K. K. In *Should we relax seismic criteria for shorter system exposure times?*, ASME Pressure Vessels and Piping Conference, Montreal, Montreal, 1996.

Elremaily, A.; Azizinamini, A., Behavior and strength of circular concrete-filled tube columns. *Journal of Constructional Steel Research* **2002,** *58*, 1567-1591.

Gerschwindner, L. F.; Leon, R. T.; Hajjar, J. F., Discussion- Limit State Response of Composite Columns and Beam-Columns Part II- Application of Design Provisions for the 2005 AISC Specification. *Engineering Journal* **2010,** *Second Quarter*, 131.

Goode, C. D., ASCCS Database of Concrete Filled Steel Tube Column Tests. 2013.

Han, L.-H.; Wang, W.-D.; Tao, Z., Performance of circular CFST column to steel beam frames under lateral cyclic loading. *Journal of Constructional Steel Research* **2011,** *67* (5), 876-890.

Hassoun, M. N.; Al-Manaseer, A., *Structural concrete: theory and design*. John Wiley & Sons: 2012.

Hill, H. J., Rational and Irrational Design Loads for Temporary Structures. *Practice Periodical on Structural Design and Construction* **2004**.

Ibarra, L. F.; Krawinkler, H. *Global Collapse of Frame Structures under Seismic Excitations*; Pacific Earthquake Engineering Research Center: 2005.

Ibarra, L. F.; Medina, R. A.; Krawinkler, H., Hysteretic models that incorporate strength and stiffness deterioration. *Earthquake Engineering & Structural Dynamics* **2005,** *34* (12), 1489-1511.

Jennings, P. C.; Husid, R., Collapse of yielding structures during earthquakes. *Journal of Engineering Mechanics* **1968**.

Ketchum, M.; Chang, V.; Shantz, T. S. *Influence of Design Ground Motion Level on Highway Bridge Costs*; Pacific Earthquake Engineering Research Center, Program of Applied Earthquake Engineering Research on Lifeline Systems: 2004.

Kitada, T., *Stability and ductility of steel structures under cyclic loading*. CRC Press: 1991; Vol. 3.

Kitada, T., *Ductility and ultimate strength of concrete-filled steel members*. CRC Press, Boca Raton, Fla: 1992.

Kitada, T., Ultimate strength and ductility of state-of-the-art concrete-filled steel bridge piers in Japan. *Engineering structures* **1998,** *20* (4), 347-354.

Knowles, R. B.; Park, R., Strength of concrete filled steel columns. *Journal of the structural division* **1969**.

Kosmatka, S. H.; Panarese, W. C., Design and control of concrete mixtures. Portland Cement Association: 2002.

Leon, R. T.; Hajjar, J. F., Limit State Response of Composite Columns and Beam-Columns Part I-Formulation of Design Provisions for the 2005 AISC Specification. *Engineering Journal* **2007,** *Fourth Quarter*, 341.

Leon, R. T.; Hajjar, J. F., Limit State Response of Composite Beam-Columns -- Part II Application. *Engineering Journal* **2008,** *45* (1).

Leon, R. T.; Perea, T.; Hajjar, J. F.; Denavit, M. D., Concrete-filled tubes columns and beam-columns a database for the AISC 2005 and 2010 specifications. **2011**.

Liel, A. B.; Haselton, C. B.; Deierlein, G. G.; Baker, J. W., Incorporating modeling uncertainties in the assessment of seismic collapse risk of buildings. *Structural Safety* **2009,** *31* (2), 197-211.

Lignos, D. G. Modified Ibarra-Medina-Krawinkler Deterioration Model with Peak-Oriented Hysteretic Response (ModIMK Peak Oriented Material). http://opensees.berkeley.edu/wiki/index.php/Modified_Ibarra-Medina-Krawinkler_ Deterioration_Model_with_Peak-Oriented_Hysteretic_Response_(ModIMKPeakOriented_Material).

Lignos, D. G.; Krawinkler, H., Deterioration Modeling of Steel Components in Support of Collapse Prediction of Steel Moment Frames under Earthquake Loading. *Journal of Structural Engineering* **2011,** *137* (11), 1291-1302.

Lignos, D. G.; Krawinkler, H. *Sidesway Collapse of Deteriorating Structural Systems Under Seismic Excitations*; Stanford University: 2012.

Mackie, K.; Wong, J.-M.; Stojadinovic, B. *Integrated Probabilistic Performance-Based Evaluation of Benchmark Reinforced Concrete Bridges*; Pacific Earthquake Engineering Research Center: College of Engineering, University of California, Berkeley, 2008.

MacRae, G. A., P-Δ effects on single-degree-of-freedom structures in earthquakes. *Earthquake Spectra* **1994,** *10* (3), 539-568.

Marson, J. Cyclic Testing of Concrete-Filled Circular Steel Tube Bridge Columns having Encased Fixed Based Detail. University of Ottawa, Ottawa, Canada, 2000.

Marson, J.; Bruneau, M., Cyclic Testing of Concrete-Filled Circular Steel Bridge Piers having Encased Fixed-Based Detail. *Journal of Bridge Engineering* **2004,** *January/February*.

McKenna, F.; Fenves, G.; Scott, M. *Open system for earthquake engineering simulation*, University of California: Berkeley, CA, 2000.

Mindess, S.; Young, J. F.; Darwin, D., *Concrete*. 2003.

Olson, D. E.; Amin, M.; Jaques, L. V. In *Evaluation of Temporary Loads: Approach to Justify Larger Loads with Less Effort*, Pressure Vessels and Piping Division (ASME), 1994.

Ranzi, G.; Leoni, G.; Zandonini, R., State of the art on the time-dependent behaviour of composite steel–concrete structures. *Journal of Constructional Steel Research* **2013,** *80*, 252-263.

Sivaselvan, M. V.; Reinhorn, A. M., Hysteretic models for deteriorating inelastic structures. *Journal of Engineering Mechanics* **2000,** *126* (6), 633-640.

Song, J.-K.; Pincheira, J. A., Spectral displacement demands of stiffness-and strength-degrading systems. *Earthquake Spectra* **2000,** *16* (4), 817-851.

Sun, C.-K.; Berg, G. V.; Hanson, R. D., Gravity effect on single-degree inelastic system. *Journal of the Engineering Mechanics Division* **1973,** *99* (1), 183-200.

Vamvatsikos, D. *IDA Matlab running routines for OpenSEES*, 2011.

Vamvatsikos, D.; Cornell, C. A., Incremental dynamic analysis. *Earthquake Engineering & Structural Dynamics* **2002,** *31* (3), 491-514.

Vamvatsikos, D.; Cornell, C. A., Applied Incremental Dynamic Analysis. *Earthquake Spectra* **2004,** *20* (2), 523-553.

Vian, D.; Bruneau, M., *Experimental investigation of P-delta effects to collapse during earthquakes*. Multidisciplinary Center for Earthquake Engineering Research: 2001.

Villaverde, R., Methods to assess the seismic collapse capacity of building structures: State of the art. *Journal of Structural Engineering* **2007,** *133* (1), 57-66.

Winters-Downey, E.; Zuo, J.; Wang, M., Hollow Product, Solid Benefit. *Modern Steel Construction* **2013**.

Zhang, J.; Denavit, M. D.; Hajjar, J.; Lu, X., Bond behavior of concrete-filled steel tube (CFT) structures. *Engineering Journal* **2012,** *49* (4), 169-185.

Zhao, X.-L.; Han, L.-H.; Lu, H., *Concrete-filled Tubular Members and Connections*. Spon Press: 2010.

APPENDIX A: COMPARATIVE CCFT DATA

Table A 1 Proposed CCFT Column as a Function of Time and Experimental CCFT Data

	CCFT28	CCFT14	CCFT7	CCFT3	CFST64	CFST51	CFST34	CFST42
D/t	64				73.89	58.88	43.18	42.78
D (in)	**39**				**16**	**12.75**	**12.75**	**16**
t (nominal) (in)	**0.61**				0.25	0.25	0.375	0.375
t (measured) (in)	-				**0.22**	**0.22**	**0.30**	**0.37**
h (in)	**264**				86.61			
A_s (in^2)	73				10.74	8.53	11.55	18.36
A_c (in^2)	1121				190.32	119.15	116.12	182.70
A_s/A_c	6.56%				5.64%	7.16%	9.95%	10.05%
I_s (in^4)	13543				334.41	167.47	224.15	560.71
I_c (in^4)	100017				2882.58	1129.74	1073.06	2656.28
P (k)	**1792**				**225**	**360**	**409**	**409**
self-weight (k)	**30**				**5**	**3**	**3**	**5**
W (k)	2369				299	472	536	539
F_y (specified) (ksi)	50				50.76	50.76	50.76	50.76
F_y (tested) (ksi)	-				64.11	58.02	60.19	73.24
F_u (ksi)	65				81.51	78.76	74.69	86.30
ε_s (tested steel strain)	-				0.0030	0.0034	0.0024	0.0043
E_s (ksi)	29000							
% concrete strength	-	90%	65%	40%	-	-	-	-
f$'_c$ (ksi)	5.2	4.68	3.38	2.08	5.35	5.09	5.88	5.09
E_c (ksi)	4552	4376	3873	3229	4603	4514	4766	4517
C_3 (AISC factor)	0.72				0.71	0.73	0.78	0.78
$EI_{eff,AISC}$ (k-in^2)	7.22E+08	7.09E+08	6.73E+08	6.26E+08	1.91E+07	8.60E+06	1.05E+07	2.57E+07
$EI_{eff,AASHTO}$ (k-in^2)	**5.749E+08**	**5.678E+08**	**5.477E+08**	**5.219E+08**	1.501E+07	6.897E+06	8.546E+06	2.106E+07
$0.8EI_{eff,AASHTO}$(k-in^2)	-	-	-	-	**1.20E+07**	**5.52E+06**	**6.84E+06**	**1.68E+07**
S_a	0.502							
V (= WS$_a$) (k)	1189				149.99	236.88	269.26	270.55
Δ_{AISC} (in)	10.10	10.29	10.84	11.65	1.70	5.97	5.56	2.28
Δ_{AASHTO} (in)	12.69	12.85	13.32	13.98	2.71	9.30	8.53	3.48
θ (= PΔ/Vh)	0.072	0.073	0.076	0.080	0.047	0.163	0.150	0.061
P_y (AISC P_n) (k)	9213	8659	7275	5890	1657	1070	1344	2229
P/P_y	0.19	0.21	0.25	0.30	0.14	0.34	0.30	0.18
M_p (AISC) (k-ft)	5258	5180	4943	4345	386	220	292	674
M_p/M_y	0.87				0.86	0.81	0.88	0.93
M_y (k-ft)	**6039.22**	**5949.38**	**5676.91**	**4989.88**	**449.91**	**271.42**	**331.90**	**722.07**
$M_{y,P-\Delta}(M_y(1-\theta))$(k-ft)	5602	5513	5245	4592	429	227	282	678
M_c/M_y	1.3							
M_c (k-ft)	7851	7734	7380	6487	585	353	431	939
F_y (= M_y/h) (k)	275	270	258	227	62.34	37.61	45.99	100.04
F_y/W	0.12	0.11	0.11	0.10	0.21	0.08	0.09	0.19
m (k-s^2/in)	4.72				0.60	0.94	1.07	1.07
k (k/in)	93.73	92.58	89.30	85.10	55.43	25.48	31.57	77.80
$T_1(2\pi(m/k)^{1/2})$(sec)	1.4101	1.4188	1.4446	1.4799	0.6511	1.2070	1.1560	0.7382
T_1(OpenSees)(sec)	1.4097	1.4185	1.4443	1.4795	0.6514	1.2069	1.1559	0.7379

bold terms implemented into concentrated plasticity model

APPENDIX B: BUCKLING ANALYSIS CALCULATIONS

Deformation of a CCFT

restart

$P_{axial} := (1792 + 30) = 1822$k (axial load applied plus self-weight)

$L := 264 :$ in

$A_s := 73 :$ in^2

$A_c := 1121 :$ in^2

$E_s := 29000 :$ ksi

$I_s := 13543 :$ in^4

$E_c := 4552 :$ ksi

$I_c := 100017 :$ in^4

Axial deformation:

$$\delta = \frac{PL}{AE} \; : \; \rightarrow \; \delta_s = \frac{P_s \cdot L}{A_s \cdot E_s} \; : \; \delta_c = \frac{P_c \cdot L}{A_c \cdot E_c} \; : \; \rightarrow \; \frac{P_s}{A_s \cdot E_s} = \frac{P_c}{A_c \cdot E_c} \; :$$

$$P_s := \frac{A_s \cdot E_s \cdot P_{axial}}{A_s \cdot E_s + A_c \cdot E_c} \; :$$

$$P_c := \frac{A_c \cdot E_c \cdot P_{axial}}{A_s \cdot E_s + A_c \cdot E_c} \; :$$

$$\delta_s := \frac{P_s \cdot L}{A_s \cdot E_s} = .066623 \text{ in.}$$

Check that $\delta_s = \delta_c$:

$$\delta_c := \frac{P_c \cdot L}{A_c \cdot E_c} = .066623 \text{ in.}$$

Bridge Column Deflection:
From Caltrans Standard Specifications 2010: http://www.dot.ca.
gov/hq/esc/oe/specifications/std_specs/2010_StdSpecs/2010_StdSpecs.pdf
55 STEEL STRUCTURES
55-1 GENERAL
55-1.01 GENERAL 55-1.01A Summary
Section 55-1 includes general specifications for furnishing and erecting structural steel or
metalwork.
Connection details for highway bridges must comply with AASHTO LRFD Bridge
Design Specifications with California Amendments.

From AASHTO LRFD Bridge Design Specifications, 2012:
2.5.2.6 - Deformations
2.5.2.6.1 - General
Bridges should be designed to avoid undesirable structural or psychological effects due to their deformations. While deflection and depth limitations are made optional, ...any large deviation from past successful practice regarding slenderness and deflections should be cause for review of the design to determine that it will perform adequately. (California made no amendments to section 2.5) http://www.dot.ca. gov/hq/esc/techpubs/manual/bridgemanuals/ca-to-aashto-lrfd-bds/caalbds_v4.html

Bridge design values below from Ketchum et al., 2004 (Bridge Type One)
Tributary dead load without self-weight: $DL := 1792$: kips

Effective Seismic Weight, W (AASHTO LRFD 3.10.9.4.3.b):
ϕ for Reinforced Concrete is 1.3
ϕ for Steel is 1.25 (for CFST using 1.3)
so, $\phi := 1.3$:
$W := \phi \cdot DL = 2330.$ k

From AASHTO LRFD 3.10 Earthquake Effects: EQ
3.10.1 - General
Bridges shall be designed to have a low probability of collapse but may suffer significant damage and disruption to service when subject to earthquake ground motions that have a seven percent probability of exceedance in 75 years.

From Lee and Billington, 2011: Assuming a site within 6.2 miles of Hayward Fault on stiff soil (site class D) and linearly interpolating to reach a 7% probability of exceedance in 75 years, or a 0.00968 mean annual frequency of exceedance,
$Sa := 0.502$: g
$P_{seismic} := W \cdot Sa = 1169.$ k

From AASHTO Guide Specifications for LRFD Seismic Bridge Design, 2011:
C7.6 (commentary for CFST for SDCD C and D):
$$EI_{eff,\,AASHTO} := E_s \cdot I_s + \frac{E_c \cdot I_c}{2.5} = 5.75 \times 10^8 \text{ k-in}^2$$
Modeling column as a fixed-end cantilever:

$$\delta_{AASHTO} := \frac{P_{seismic} \cdot L^3}{3 \cdot EI_{eff,\,AASHTO}} = 12.48 \text{ in}$$

From AISC Steel Construction Manual, Eq. I2-12 (pg 16.1-88):
$$C_3 := \min\left(0.6 + 2\left(\frac{A_s}{A_c + A_s}\right), 0.9\right) = 0.7222780570$$
$I_{sr} := 0$: (no reinforcing bar)

$$EI_{eff,\,AISC} := E_s \cdot I_s + E_s \cdot I_{sr} + C_3 \cdot E_c \cdot I_c = 7.22 \times 10^8 \text{k-in}^2$$
Modeling column as a fixed-end cantilever:

$$\delta_{AISC} := \frac{P_{seismic} \cdot L^3}{3 \cdot EI_{eff, AISC}} = 9.94 \text{ in}$$

As compared with 48" diameter Reinforced Concrete:
From ACI 318-11:
10.10.4.1 (Elastic second-order analysis)...Columns=0.70*I

$$I_{RC} := 0.70 \cdot (260576) = 182403. \text{in}^4$$

$$\delta := \frac{P_{seismic} \cdot L^3}{3 \cdot E_c \cdot I_{RC}} = 8.64 \text{ in}$$

APPENDIX C: INTERACTION DIAGRAM CALCULATIONS

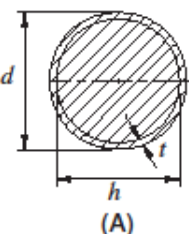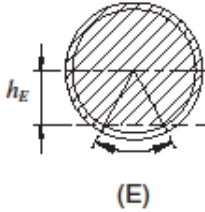Table C 1 P-M Capacities of CCFT

(Gerschwindner et al., 2010)
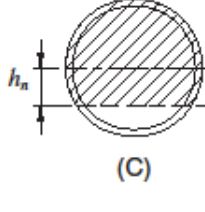
Table D.
Plastic Capacities for Composite, Filled Round HSS
Bent About Any Axis

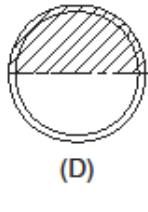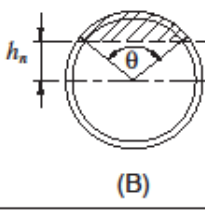| Section	Stress Distribution	Point	Defining Equations
(A) d, t, h	$0.95f'_c$ F_y	A	$P_A = F_y A_s + 0.95 f'_c A_c$ * $M_A = 0$ $A_s = \pi(dt - t^2)$ $A_c = \dfrac{\pi h^2}{4}$
(E) h_E PNA		E	$P_E = P_A - \tfrac{1}{4}\left[F_y\left(d^2 - h^2\right) + \tfrac{1}{2}\left(0.95 f'_c\right)h^2\right]\left(\theta_2 - \sin\theta_2\right)$ $M_E = F_y Z_{sE} + \tfrac{1}{2}\left(0.95 f'_c Z_{cE}\right)$ $Z_{cE} = \dfrac{h^3}{6}\sin^3\left(\dfrac{\theta_2}{2}\right)$ $Z_{sE} = \dfrac{\left(d^3 - h^3\right)}{6}\sin\left(\dfrac{\theta_2}{2}\right)$ $h_E = \dfrac{h_n}{2} + \dfrac{h}{4}$ $\theta_2 = \pi - 2\arcsin\left(\dfrac{2h_E}{h}\right)$
(C) h_n PNA		C	$P_C = 0.95 f'_c A_c$ $M_C = M_B$
(D) h_n PNA		D	$P_D = \dfrac{0.95 f'_c A_c}{2}$ $M_D = F_y Z_s + \tfrac{1}{2}\left(0.95 f'_c Z_c\right)$ $Z_s = \text{plastic section modulus of steel shape} = \dfrac{d^3}{6} - Z_c$ $Z_c = \dfrac{h^3}{6}$
(B) h_n θ PNA		B	$P_B = 0$ $M_B = F_y Z_{sB} + \tfrac{1}{2}\left(0.95 f'_c Z_{cB}\right)$ $Z_{sB} = \dfrac{\left(d^3 - h^3\right)}{6}\sin\left(\dfrac{\theta}{2}\right)$ $Z_{cB} = \dfrac{h^3 \sin^3\left(\dfrac{\theta}{2}\right)}{6}$ $\theta = \dfrac{0.0260 K_c - 2K_s}{0.0848 K_c}$ $+ \dfrac{\sqrt{\left(0.0260 K_c + 2K_s\right)^2 + 0.857 K_c K_s}}{0.0848 K_c}$ (rad) $K_c = f'_c h^2$ $K_s = F_y\left(\dfrac{d-t}{2}\right)$ ("thin" HSS wall assumed) $h_n = \dfrac{h}{2}\sin\left(\dfrac{\pi - \theta}{2}\right) \le \dfrac{h}{2}$

*0.95f'_c may be used for concrete filled round HSS.

Table C 2 Calculated P-M Parameters of Proposed CCFT Column

54

	CCFT28	CCFT14	CCFT7	CCFT3
d (D) (in)	39	39	39	39
t (in)	0.61	0.61	0.61	0.61
h (in)	37.78	37.78	37.78	37.78
h_n (in)	8.6	8.2	6.9	5.2
h_E (in)	13.7	13.5	12.9	12.0
F_y (ksi)	50	50	50	50
F_u (ksi)	65	65	65	65
E_s (ksi)	29000	29000	29000	29000
A_s (in^2)	73	73	73	73
I_s (in^4)	13543	13543	13543	13543
Z_s (in^3)	898	898	898	898
Z_{sB} (in^3)	801	810	836	864
Z_{sE} (in^3)	617	627	656	693
S_s (in^3)	695	695	695	695
K_s (k/in)	585	585	585	585
$K_{nominal}$	1	1	1	1
r_s (in)	13.6	13.6	13.6	13.6
L (h) (in)	264	264	264	264
F_e	757	757	757	757
F_{cr}	48.6	48.6	48.6	48.6
θ (rad)	2.20	2.25	2.39	2.59
θ_2 (rad)	1.51	1.55	1.64	1.76
d_c (in)	37.78	37.78	37.78	37.78
A_c (in^2)	1121	1121	1121	1121
I_c (in^4)	100017	100017	100017	100017
f'_c (ksi)	5.20	4.68	3.38	2.08
w_c (lbs/cf)	145	145	145	145
$*E_c$ (ksi)	4552	4376	3873	3229
Z_c (in^3)	8988	8988	8988	8988
Z_{cB} (in^3)	6363	6597	7252	8004
Z_{cE} (in^3)	2913	3060	3509	4126
K_c (k/in)	7423	6680	4825	2969
Q (in^3)	449	449	449	449
Z (in^3)	898	898	898	898

Table C 3 Calculated P-M Capacities of Proposed CCFT and Design Basis RC Columns

Leon/Hajjar (AISC)   ACI

	CCFT28		CCFT14		CCFT7		CCFT3		RC		AISC (ACI)
	P_n (k)	M_n (k-ft)	P_n (k)	M_n (k-ft)	P_n (k)	M_n (k-ft)	P_n (k)	M_n (k-ft)	P_n (k)	M_n (k-ft)	
A	9213	0	8659	0	7275	0	5890	0	10259	0	A (A)
E	6790	3170	6287	3180	5054	3205	3877	3227	3357	5591	E (B)
C	5538	4645	4984	4598	3600	4454	2215	4260			
D	2769	5593	2492	5408	1800	4945	1108	4483	3346	5585	D (C)
B	0	4645	0	4598	0	4454	0	4260	1442	4977	(CD)
linear interpolation to determine where on curve the applied axial load falls:									1281	4866	(D)
	1792	5258.4	1792	5180.2	1792	4943	1792	4344.8	-88	3347	(E)
									-2418	0	(F)

56

Table C 4 Reinforced Concrete Column Data for Design-basis Bridge

(Mackie et al., 2008)

Input Variable (name)	Description and Computation
column diameter	outer diameter of a circular column
column surface area	
number of columns	total count of columns in single bent configuration
required column casing thickness	thickness of column casing based on diameter of column and Caltrans detail sheet XS7-010e
column height	total column height from pile cap to bottom of superstructure
bar area	total cross-sectional area of longitudinal steel in the column
diameter of longitudinal bars	diameter of longitudinal steel
number of longitudinal bars	total count of individual longitudinal steel bars
percent transverse reinforcement	
percent long. reinforcement	
column dead load (bottom)	gravity dead load at the bottom of the column, including the self-weight of the column
col gross area (A_g)	(column diameter)$^2 \times \pi$
column cover	minimum cover from outside of transverse steel hoops
total column bar volume (long.)	total volume of longitudinal bars calculated using nominal area
total column bar weight (long.)	total weight of longitudinal bars calculated using nominal weight per foot
steel (f_{ye})	yield stress of bar reinforcing steel
concrete (f'_{ce})	compressive strength of concrete at 28 days
steel weight	unit weight of reinforcing steel
concrete weight	unit weight of concrete
steel weight estimate (BDA 11-5)	total weight of reinforcing steel per volume assumed for estimating purposes
total column gross volume	gross volume computed using $A_g \times$ (column height)

Input Variable (name)	Value (value, unit)		Metric Value		Notes
column diameter	48	in.	1.22	m	
column surface area	276	sf	25.68	m^2	
number of columns	4	ea	4	ea	
required column casing thickness	0.375	in.	0.0095	m	XS7-010e
column height	22	ft	6.706	m	
bar area	1.27	in.^{2}	0.00082	m^2	US #10 bars
diameter of longitudinal bars	1.272	in.	0.0323	m	US #10 bars
number of longitudinal bars	28	ea	28	ea	
percent transverse reinforcement	1.59	%	1.59	%	
percent long. reinforcement	2.0	%	2.0	%	
column dead load (bottom)	1837	k	8171	kN	
col gross area (A_g)	1810	in.^{2}	1.168	m^2	
column cover	1.5	in.	0.038	m	
total column bar volume (long.)	5.43	cf	0.154	m^3	
total column bar weight (long.)	2662	lb	1207	kg	
steel (f_{ye})	68	ksi	468843	kPa	
concrete (f'_{ce})	5.20	ksi	35853	kPa	
steel weight	490	lb/ft^3	76973	N/m^3	
concrete weight	150	lb/ft^3	23563	N/m^3	
steel weight estimate (BDA 11-5)	16.72	lb/ft^3	268.0	kg/m^3	BDA 11-5
total column gross volume	276.53	ft^3	7.826	m^3	

Interaction Curve Calculations of Reinforced Concrete Column

restart
$dia_{col} := 48 :$

$rad_{col} := \dfrac{dia_{col}}{2} = 24$

$A_g := evalf(\pi) \cdot \left(\dfrac{dia_{col}}{2} \right)^2 = 1809.56$

$h_{col} := 264 :$
$cover := 1.5 :$
$dia_{stl} := 1.272 :$
$a_{stl} := 1.27 :$
$numberofbars := 28 :$
$A_{stl} := numberofbars \cdot a_{stl} = 35.56$
$f_{cprime} := 5.2 :$
$f_y := 68. :$
$E_s := 29000 :$
$\epsilon_{cu} := 0.003 :$

$\epsilon_y := \dfrac{f_y}{E_s} = .00$

Point A

$P_{n,A} := \left(0.85 \cdot f_{cprime} \cdot (A_g - A_{stl}) + f_y \cdot A_{stl} \right) = 10259.15$

$M_{n,A} := 0 :$

$\phi P_{n,A} := 0.75 \cdot \left(0.85 \cdot f_{cprime} \cdot (A_g - A_{stl}) + f_y \cdot A_{stl} \right) = 7694.36$

$\phi P_{n,maximum} := 0.85 \cdot 0.75 \cdot \left(0.85 \cdot f_{cprime} \cdot (A_g - A_{stl}) + f_y \cdot A_{stl} \right) = 6540.21$

$\phi M_{n,A} := 0 :$

Point C

$$dia_{reinf} := dia_{col} - 2 \cdot \left(cover + \left(\frac{dia_{stl}}{2} \right) \right) = 43.73$$

$$rad_{reinf} := \frac{dia_{reinf}}{2} = 21.86$$

$$circumferance_{reinf} := dia_{reinf} \, evalf(\pi) = 137.38$$

$$spacing_{stl} := \frac{circumferance_{reinf}}{numberofbars} = 4.91 \text{ (arc length,s)}$$

Sample calculation to calculate d1:

$$\theta_1 := \frac{spacing_{stl}}{(rad_{reinf})} = .22 \text{ (central angle)}$$

$$h_{segment,\,1} := rad_{reinf} \left(1 - \cos\left(\frac{\theta_1}{2} \right) \right) = .14 \text{ (segment height, h)}$$

$$d_1 := cover + \frac{dia_{stl}}{2} + h_{segment,\,1} = 2.27 \text{ (this is the smallest d value, to the reinforcing at}$$

top)

Similarly, calculate d1 through dn

$$d_n := cover + \frac{dia_{stl}}{2} + rad_{reinf} \left(1 - \cos\left(\frac{\frac{(2 \cdot n - 1) \cdot spacing_{stl}}{(rad_{reinf})}}{2} \right) \right) :$$

for k **from** 1 **by** 1 **to** 14 **do** $d_k := evalf\left(subs\left(n = k, d_n \right) \right)$ **od**:

$$Z_C := -1 :$$

$$\epsilon_{14} := Z_C \cdot \epsilon_y = -2.34 \times 10^{-3}$$

$$c := \frac{\epsilon_{cu}}{\epsilon_{cu} - Z_C \cdot \epsilon_y} \cdot d_{14} = 25.67$$

Sample, to calculate strain at 13, and 12:

$$\epsilon_{13} := \frac{(c - d_{13})}{c} \cdot \epsilon_{cu} = -2.22 \times 10^{-3}$$

$$\epsilon_{12} := \frac{(c - d_{12})}{c} \cdot \epsilon_{cu} = -1.97 \times 10^{-3}$$

Similarly, to calculate all of the remaining strains:

$$\epsilon_n := \frac{(c - d_n)}{c} \cdot \epsilon_{cu} :$$

for k **from** 1 **by** 1 **to** 14 **do** $\epsilon_k := evalf\left(subs\left(n = k, \epsilon_n \right) \right)$ **od**:

To calculate stress in 14:

$$f_{14} := \max\left(\epsilon_{14} \cdot E_s, -f_y \right) = -68.00$$

Similarly, to calculate the remaining stresses:

$$f_n := \max\left(\epsilon_n \cdot E_s, -f_y \right) :$$

for k **from** 1 **by** 1 **to** 14 **do** $f_k := evalf\left(subs\left(n = k, f_n \right) \right)$ **od**:

$$\beta := 0.85 - 0.05 \cdot \frac{\left(f_{cprime} \cdot 1000 - 4000\right)}{1000} = .79$$

$$stressblockheight := \beta \cdot c = 20.28$$

$$\theta_C := 2 \cdot \arccos\left(\frac{rad_{col} - stressblockheight}{rad_{col}}\right) = 2.83$$

$$stressblockarea := \frac{rad_{col}^2}{2} \cdot \left(\theta_C - \sin\left(\theta_C\right)\right) = 726.75$$

$$C_C := 0.85 \cdot f_{cprime} \cdot stressblockarea = 3212.22$$

To calculate force in rebar at level 14 (2 bars ea. level)

if $stressblockheight < d_{14}$ **then** $F_{14} := f_{14} \cdot \left(2 \cdot a_{stl}\right)$ **else** $F_{14} := \left(f_{14} - 0.85 \cdot f_{cprime}\right) \cdot \left(2 \cdot a_{stl}\right)$ **end**

$$= -172.72$$

Similarly, to calculate all of the forces, where in this case d6<stressblockheight<d7

$$F_n := \left(f_n - 0.85 \cdot f_{cprime}\right) \cdot \left(2 \cdot a_{stl}\right) :$$

for k **from** 1 **by** 1 **to** 6 **do** $F_k := evalf\left(subs\left(n = k, F_n\right)\right)$ **od**:

$$F_n := f_n \cdot \left(2 \cdot a_{stl}\right) :$$

for k **from** 7 **by** 1 **to** 14 **do** $F_k := evalf\left(subs\left(n = k, F_n\right)\right)$ **od**:

$$P_{n, C} := C_C + add\left(F_n, n = 1..14\right) = 3345.66$$

centroid of stress block

$$centroidstressblockC := \frac{4 \cdot rad_{col} \cdot \sin^3\left(\frac{\theta_C}{2}\right)}{3 \cdot \left(\theta_C - \sin\left(\theta_C\right)\right)} = 12.23$$

$$M_{n, C} := \frac{\left(\left(C_C \cdot centroidstressblockC\right) + add\left(F_n \cdot \left(rad_{col} - d_n\right), n = 1..14\right)\right)}{12} =$$

5584.546710

if $-0.002 < \epsilon_{14} < 0.003$ **then** $\phi := 0.75$ **elif** $-0.005 < \epsilon_{14} < -0.002$ **then** $\phi := 0.75 + \left(-\epsilon_{14} - 0.002\right) \cdot 50$ **elif** $\epsilon_{14} \leq -0.005$ **then** $\phi := 0.90$ **end**

$$= .77$$

$$\phi P_{n, C} := \phi \cdot P_{n, C} = 2566.93$$

$$\phi M_{n, C} := \phi \cdot M_{n, C} = 4284.69$$

Point CD (transitional between C and D)

$$Z_{CD} := -2 :$$

$$\epsilon_{14} := Z_{CD} \cdot \epsilon_y = -4.69 \times 10^{-3}$$

$$c := \frac{\epsilon_{cu}}{\epsilon_{cu} - Z_{CD} \cdot \epsilon_y} \cdot d_{14} = 17.84$$

Sample, to calculate strain at 13, and 12:

$$\epsilon_{13} := \frac{(c - d_{13})}{c} \cdot \epsilon_{cu} = -4.51 \times 10^{-3}$$

$$\epsilon_{12} := \frac{(c - d_{12})}{c} \cdot \epsilon_{cu} = -4.15 \times 10^{-3}$$

Similarly, to calculate all of the remaining strains:

$$\epsilon_n := \frac{(c - d_n)}{c} \cdot \epsilon_{cu} :$$

for k **from** 1 **by** 1 **to** 14 **do** $\epsilon_k := evalf\big(subs(n = k, \epsilon_n)\big)$ **od**:

To calculate stress in 14:

$$f_{14} := \max\big(\epsilon_{14} \cdot E_s - f_y\big) = -68.$$

Similarly, to calculate the remaining stresses:

$$f_n := \max\big(\epsilon_n \cdot E_s - f_y\big) :$$

for k **from** 1 **by** 1 **to** 14 **do** $f_k := evalf\big(subs(n = k, f_n)\big)$ **od**:

$$\beta := 0.85 - 0.05 \cdot \frac{(f_{cprime} \cdot 1000 - 4000)}{1000} = .79$$

$$stressblockheight := \beta \cdot c = 14.09$$

$$\theta_{CD} := 2 \cdot \arccos\left(\frac{rad_{col} - stressblockheight}{rad_{col}}\right) = 2.29$$

$$stressblockarea := \frac{rad_{col}^2}{2} \cdot \big(\theta_{CD} - \sin(\theta_{CD})\big) = 443.12$$

$$C_{CD} := 0.85 \cdot f_{cprime} \cdot stressblockarea = 1958.61$$

To calculate force in rebar at level 14 (2 bars ea. level)

if $stressblockheight < d_{14}$ **then** $F_{14} := f_{14} \cdot (2 \cdot a_{stl})$ **else** $F_{14} := \big(f_{14} - 0.85 \cdot f_{cprime}\big) \cdot (2 \cdot a_{stl})$ **end**

$$= -172.72$$

Similarly, to calculate all of the forces, where in this case d6<stressblockheight<d7

$$F_n := \big(f_n - 0.85 \cdot f_{cprime}\big) \cdot (2 \cdot a_{stl}) :$$

for k **from** 1 **by** 1 **to** 5 **do** $F_k := evalf\big(subs(n = k, F_n)\big)$ **od**:

$$F_n := f_n \cdot (2 \cdot a_{stl}) :$$

for k **from** 6 **by** 1 **to** 14 **do** $F_k := evalf\big(subs(n = k, F_n)\big)$ **od**:

$$P_{n,CD} := C_{CD} + add(F_n, n = 1..14) = 1441.76$$

centroid of stress block

$$centroidstressblockCD := \frac{4 \cdot rad_{col} \cdot \sin^3\left(\frac{\theta_{CD}}{2}\right)}{3 \cdot \big(\theta_{CD} - \sin(\theta_{CD})\big)} = 15.71$$

$$M_{n,CD} := \frac{\big(\big(C_{CD} \cdot centroidstressblockCD\big) + add\big(F_n \cdot (rad_{col} - d_n), n = 1..14\big)\big)}{12} = 4976.60$$

if $-0.002 < \epsilon_{14} < 0.003$ **then** $\phi := 0.75$ **elif** $-0.005 < \epsilon_{14} < -0.002$ **then** $\phi := 0.75 +$ (

$$-\epsilon_{14} - 0.002\big) \cdot 50 \textbf{ elif } \epsilon_{14} \leq -0.005 \textbf{ then } \phi := 0.90 \textbf{ end}$$

$= .88$

$\phi P_{n,\,CD} := \phi \cdot P_{n,\,CD} = 1275.21$

$\phi M_{n,\,CD} := \phi \cdot M_{n,\,CD} = 4401.72$

Point D (tension-controlled point)

$\epsilon_{14} := -0.005 :$

$c := \dfrac{\epsilon_{cu}}{\epsilon_{cu} - \epsilon_{14}} \cdot d_{14} = 17.15$

Sample, to calculate strain at 13, and 12:

$\epsilon_{13} := \dfrac{(c - d_{13})}{c} \cdot \epsilon_{cu} = -4.81 \times 10^{-3}$

$\epsilon_{12} := \dfrac{(c - d_{12})}{c} \cdot \epsilon_{cu} = -4.44 \times 10^{-3}$

Similarly, to calculate all of the remaining strains:

$\epsilon_n := \dfrac{(c - d_n)}{c} \cdot \epsilon_{cu} :$

for k **from** 1 **by** 1 **to** 14 **do** $\epsilon_k := evalf\big(subs\big(n = k, \epsilon_n\big)\big)$**od**:

To calculate stress in 14:

$f_{14} := \max\big(\epsilon_{14} \cdot E_s\text{-}f_y\big) = -68.$

Similarly, to calculate the remaining stresses:

$f_n := \max\big(\epsilon_n \cdot E_s\text{-}f_y\big) :$

for k **from** 1 **by** 1 **to** 14 **do** $f_k := evalf\big(subs\big(n = k, f_n\big)\big)$**od**:

$\beta := 0.85 - 0.05 \cdot \dfrac{(f_{cprime} \cdot 1000 - 4000)}{1000} = .79$

$stressblockheight := \beta \cdot c = 13.55$

$\theta_D := 2 \cdot \arccos\left(\dfrac{rad_{col} - stressblockheight}{rad_{col}}\right) = 2.24$

$stressblockarea := \dfrac{rad_{col}^2}{2} \cdot \big(\theta_D - \sin(\theta_D)\big) = 419.36$

$C_D := 0.85 \cdot f_{cprime} \cdot stressblockarea = 1853.57$

To calculate force in rebar at level 14 (2 bars ea. level)

if $stressblockheight < d_{14}$ **then** $F_{14} := f_{14} \cdot \big(2 \cdot a_{stl}\big)$ **else** $F_{14} := \big(f_{14} - 0.85 \cdot f_{cprime}\big) \cdot \big(2 \cdot a_{stl}\big)$ **end**

$= -172.72$

Similarly, to calculate all of the forces, where in this case d6<stressblockheight<d7

$F_n := \big(f_n - 0.85 \cdot f_{cprime}\big) \cdot \big(2 \cdot a_{stl}\big) :$

for k **from** 1 **by** 1 **to** 5 **do** $F_k := evalf\big(subs\big(n = k, F_n\big)\big)$**od**:

$F_n := f_n \cdot \big(2 \cdot a_{stl}\big) :$

for k **from** 6 **by** 1 **to** 14 **do** $F_k := evalf\left(subs\left(n=k, F_n\right)\right)$ **od**:

$P_{n,\,D} := C_D + add\left(F_n, n=1..14\right) = 1281.37$

centroid of stress block

$$centroidstressblockD := \frac{4 \cdot rad_{col} \cdot \sin^3\left(\dfrac{\theta_D}{2}\right)}{3 \cdot \left(\theta_D - \sin\left(\theta_D\right)\right)} = 16.03$$

$$M_{n,\,D} := \frac{\left(\left(C_D \cdot centroidstressblockD\right) + add\left(F_n \cdot \left(rad_{col} - d_n\right), n=1..14\right)\right)}{12} =$$

4866.46

if $-0.002 < \epsilon_{14} < 0.003$ **then** $\phi := 0.75$ **elif** $-0.005 < \epsilon_{14} < -0.002$ **then** $\phi := 0.75 + \big($
$\quad -\epsilon_{14} - 0.002\big) \cdot 50$ **elif** $\epsilon_{14} \leq -0.005$ **then** $\phi := 0.90$ **end**
$= 0.90$

$\phi P_{n,\,D} := \phi \cdot P_{n,\,D} = 1153.23$

$\phi M_{n,\,D} := \phi \cdot M_{n,\,D} = 4379.82$

Point B (zero stress in tension reinforcement point)

$Z_B := 0:$

$\epsilon_{14} := Z_B \cdot \epsilon_y = 0.$

$c := \dfrac{\epsilon_{cu}}{\epsilon_{cu} - Z_C \cdot \epsilon_y} \cdot d_{14} = 25.67$

Sample, to calculate strain at 13, and 12:

$\epsilon_{13} := \dfrac{\left(c - d_{13}\right)}{c} \cdot \epsilon_{cu} = -2.22 \times 10^{-3}$

$\epsilon_{12} := \dfrac{\left(c - d_{12}\right)}{c} \cdot \epsilon_{cu} = -1.97 \times 10^{-3}$

Similarly, to calculate all of the remaining strains:

$\epsilon_n := \dfrac{\left(c - d_n\right)}{c} \cdot \epsilon_{cu}:$

for k **from** 1 **by** 1 **to** 14 **do** $\epsilon_k := evalf\left(subs\left(n=k, \epsilon_n\right)\right)$ **od**:

To calculate stress in 14:

$f_{14} := \max\left(\epsilon_{14} \cdot E_s, -f_y\right) = -68.00$

Similarly, to calculate the remaining stresses:

$f_n := \max\left(\epsilon_n \cdot E_s, -f_y\right):$

for k **from** 1 **by** 1 **to** 14 **do** $f_k := evalf\left(subs\left(n=k, f_n\right)\right)$ **od**:

$\beta := 0.85 - 0.05 \cdot \dfrac{\left(f_{cprime} \cdot 1000 - 4000\right)}{1000} = .79$

$stressblockheight := \beta \cdot c = 20.28$

$$\theta_B := 2 \cdot \arccos\left(\frac{rad_{col} - stressblockheight}{rad_{col}}\right) = 2.83$$

$$stressblockarea := \frac{rad_{col}^2}{2} \cdot \left(\theta_B - \sin\left(\theta_B\right)\right) = 726.75$$

$$C_B := 0.85 \cdot f_{cprime} \cdot stressblockarea = 3212.22$$

To calculate force in rebar at level 14 (2 bars ea. level)

if $stressblockheight < d_{14}$ **then** $F_{14} := f_{14} \cdot \left(2 \cdot a_{stl}\right)$ **else** $F_{14} := \left(f_{14} - 0.85 \cdot f_{cprime}\right) \cdot \left(2 \cdot a_{stl}\right)$ **end**

$= -172.72$

Similarly, to calculate all of the forces, where in this case d6<stressblockheight<d7

$$F_n := \left(f_n - 0.85 \cdot f_{cprime}\right) \cdot \left(2 \cdot a_{stl}\right) :$$

for k **from** 1 **by** 1 **to** 5 **do** $F_k := evalf\left(subs\left(n = k, F_n\right)\right)$ **od**:

$$F_n := f_n \cdot \left(2 \cdot a_{stl}\right) :$$

for k **from** 6 **by** 1 **to** 14 **do** $F_k := evalf\left(subs\left(n = k, F_n\right)\right)$ **od**:

$$P_{n, B} := C_B + add\left(F_n, n = 1 ..14\right) = 3356.89$$

centroid of stress block

$$centroidstressblockB := \frac{4 \cdot rad_{col} \cdot \sin^3\left(\frac{\theta_B}{2}\right)}{3 \cdot \left(\theta_B - \sin\left(\theta_B\right)\right)} = 12.23$$

$$M_{n, B} := \frac{\left(\left(C_B \cdot centroidstressblockB\right) + add\left(F_n \cdot \left(rad_{col} - d_n\right), n = 1 ..14\right)\right)}{12} =$$

5591.30

if $-0.002 < \epsilon_{14} < 0.003$ **then** $\phi := 0.75$ **elif** $-0.005 < \epsilon_{14} < -0.002$ **then** $\phi := 0.75 + \left(-\epsilon_{14} - 0.002\right) \cdot 50$ **elif** $\epsilon_{14} \leq -0.005$ **then** $\phi := 0.90$ **end**

$= .77$

$$\phi P_{n, B} := \phi \cdot P_{n, B} = 2575.54$$

$$\phi M_{n, B} := \phi \cdot M_{n, B} = 4289.88$$

Point E

$$Z_E := -4 :$$

$$\epsilon_{14} := Z_E \cdot \epsilon_y = -9.38 \times 10^{-3}$$

$$c := \frac{\epsilon_{cu}}{\epsilon_{cu} - Z_E \cdot \epsilon_y} \cdot d_{14} = 11.08$$

Sample, to calculate strain at 13, and 12:

$$\epsilon_{13} := \frac{\left(c - d_{13}\right)}{c} \cdot \epsilon_{cu} = -9.08 \times 10^{-3}$$

$$\epsilon_{12} := \frac{(c - d_{12})}{c} \cdot \epsilon_{cu} = -8.51 \times 10^{-3}$$

Similarly, to calculate all of the remaining strains:

$$\epsilon_n := \frac{(c - d_n)}{c} \cdot \epsilon_{cu} :$$

for k **from** 1 **by** 1 **to** 14 **do** $\epsilon_k := evalf\left(subs\left(n = k, \epsilon_n\right)\right)$**od:**

To calculate stress in 14:

$$f_{14} := \max\left(\epsilon_{14} \cdot E_s - f_y\right) = -68.$$

Similarly, to calculate the remaining stresses:

$$f_n := \max\left(\epsilon_n \cdot E_s - f_y\right) :$$

for k **from** 1 **by** 1 **to** 14 **do** $f_k := evalf\left(subs\left(n = k, f_n\right)\right)$**od:**

$$\beta := 0.85 - 0.05 \cdot \frac{\left(f_{cprime} \cdot 1000 - 4000\right)}{1000} = .79$$

$$stressblockheight := \beta \cdot c = 8.75$$

$$\theta_E := 2 \cdot \arccos\left(\frac{rad_{col} - stressblockheight}{rad_{col}}\right) = 1.76$$

$$stressblockarea := \frac{rad_{col}^2}{2} \cdot \left(\theta_E - \sin\left(\theta_E\right)\right) = 225.72$$

$$C_E := 0.85 \cdot f_{cprime} \cdot stressblockarea = 997.68$$

To calculate force in rebar at level 14 (2 bars ea. level)

if $stressblockheight < d_{14}$ **then** $F_{14} := f_{14} \cdot \left(2 \cdot a_{stl}\right)$ **else** $F_{14} := \left(f_{14} - 0.85 \cdot f_{cprime}\right) \cdot \left(2 \cdot a_{stl}\right)$ **end**

$$= -172.72$$

Similarly, to calculate all of the forces, where in this case d6<stressblockheight<d7

$$F_n := \left(f_n - 0.85 \cdot f_{cprime}\right) \cdot \left(2 \cdot a_{stl}\right) :$$

for k **from** 1 **by** 1 **to** 5 **do** $F_k := evalf\left(subs\left(n = k, F_n\right)\right)$**od:**

$$F_n := f_n \cdot \left(2 \cdot a_{stl}\right) :$$

for k **from** 6 **by** 1 **to** 14 **do** $F_k := evalf\left(subs\left(n = k, F_n\right)\right)$**od:**

$$P_{n, E} := C_E + add\left(F_n, n = 1..14\right) = -87.68$$

centroid of stress block

$$centroidstressblockE := \frac{4 \cdot rad_{col} \cdot \sin^3\left(\frac{\theta_E}{2}\right)}{3 \cdot \left(\theta_E - \sin\left(\theta_E\right)\right)} = 18.81$$

$$M_{n, E} := \frac{\left(\left(C_E \cdot centroidstressblockD\right) + add\left(F_n \cdot \left(rad_{col} - d_n\right), n = 1..14\right)\right)}{12} =$$

3347.34

if $-0.002 < \epsilon_{14} < 0.003$ **then** $\phi := 0.75$ **elif** $-0.005 < \epsilon_{14} < -0.002$ **then** $\phi := 0.75 + \left(-\epsilon_{14} - 0.002\right) \cdot 50$ **elif** $\epsilon_{14} \leq -0.005$ **then** $\phi := 0.90$ **end**

$$= 0.90$$

$$\phi P_{n,E} := \phi \cdot P_{n,E} = -78.91$$

$$\phi M_{n,E} := \phi \cdot M_{n,E} = 3012.61$$

Point F (axial tension, moment equals zero point)

to calculate stresses:

$$f_n := f_y :$$

for k **from** 1 **by** 1 **to** 14 **do** $f_k := evalf\left(subs\left(n = k, f_n\right)\right)$**od**:

to calculate all of the forces,

$$F_n := -f_n \cdot \left(2 \cdot a_{stl}\right) :$$

for k **from** 1 **by** 1 **to** 14 **do** $F_k := evalf\left(subs\left(n = k, F_n\right)\right)$**od**:

$$P_{n,F} := add\left(F_n, n = 1 .. 14\right) = -2418.08$$

$$M_{n,F} := 0 = 0$$

if $-0.002 < \epsilon_{14} < 0.003$ **then** $\phi := 0.75$ **elif** $-0.005 < \epsilon_{14} < -0.002$ **then** $\phi := 0.75 + ($

$\quad -\epsilon_{14} - 0.002) \cdot 50$ **elif** $\epsilon_{14} \le -0.005$ **then** $\phi := 0.90$ **end**

$$= 0.90$$

$$\phi P_{n,F} := \phi \cdot P_{n,F} = -2176.27$$

$$\phi M_{n,F} := \phi \cdot M_{n,F} = 0.$$